

# Chapter 17

# Future Directions and Emerging Frontiers

*The Roadmap to  $\Gamma_{\text{inv}} \rightarrow 1$  and Beyond*

## QFI Gate: Chapter 17 Objectives

This capstone chapter charts the future of Quantum Field Imaging through rigorous technical analysis of emerging technologies. Each section follows a systematic structure: Motivation → Setup → Derivation → Key Result → Figure Interpretation → Design Implications.

**Part A—Algorithmic Frontiers:** How can we improve the reconstruction operator  $\mathcal{R}$ ?

- Section 17.1: The reconstruction bottleneck and  $\Gamma_{\text{inv}}$  decomposition
- Section 17.2: Physics-informed neural networks
- Section 17.3: Quantum-enhanced algorithms (VQE/QAOA)

**Part B—Sensor Frontiers:** How can we improve the measurement operator  $\mathcal{M}$ ?

- Section 17.4: Entanglement-enhanced parallel sensing
- Section 17.5: Quantum error correction for sensor arrays
- Section 17.6: Next-generation color centers

**Part C—System Frontiers:** What paradigm shifts are possible?

- Section 17.7: Neuromorphic quantum sensors
- Section 17.8: Distributed quantum sensing networks
- Section 17.9: Quantum-classical hybrid architectures

**Part D—Applications and Roadmap:**

- Section 17.10: Emerging applications and market analysis
- Section 17.11: Technology roadmap to  $\Gamma_{\text{inv}} \rightarrow 1$

**Central Question:** Which technologies will most effectively push  $Q_{\text{FOM}}$  beyond current limits, and when?

## Abbreviated Terms

Abbrev.	Full Term	Abbrev.	Full Term
CRB	Cramér-Rao Bound	QAOA	Quantum Approx. Optimization Alg.
DQSN	Distributed Quantum Sensing Network	QEC	Quantum Error Correction
FIM	Fisher Information Matrix	QFI	Quantum Field Imaging
GHZ	Greenberger-Horne-Zeilinger state	QUBO	Quadratic Unconstrained Binary Opt.
HL	Heisenberg Limit	SiV	Silicon-Vacancy Center
HHL	Harrow-Hassidim-Lloyd algorithm	SQL	Standard Quantum Limit
PINN	Physics-Informed Neural Network	SVD	Singular Value Decomposition
NMSE	Normalized Mean Square Error	$g_{\text{net}}$	Net-gain factor (overhead-adjusted)

Table 17.1: Abbreviated terms used in Chapter 17.

## Abstract

This chapter provides a technically rigorous roadmap for advancing Quantum Field Imaging from its current state ( $\Gamma_{\text{inv}} \approx 0.85$ ) toward the theoretical limit ( $\Gamma_{\text{inv}} \rightarrow 1$ ). Unlike survey-style future directions, each technology is analyzed through: (1) first-principles derivation of the governing equations, (2) quantitative performance bounds, (3) worked examples with realistic parameters, and (4) explicit figure interpretation linking theory to visualization. We identify four breakthrough technologies with the highest impact potential: physics-informed neural networks (near-term,  $\Gamma_{\text{inv}}^{\text{algo}} \rightarrow 0.95$ ), entanglement-enhanced sensing (medium-term,  $\sqrt{N}$  improvement), quantum error correction for sensors (medium-term,  $100\times$  coherence extension), and quantum holographic reconstruction (long-term,  $\sqrt{\kappa}$  advantage). All performance claims include the net-gain factor  $g_{\text{net}}$  that accounts for realistic overhead. The chapter concludes with a 15-year roadmap projecting QFI market growth based on technology readiness analysis.

## Part A: Algorithmic Frontiers

The reconstruction operator  $\mathcal{R}$  transforms measured data  $D$  into source estimates  $\hat{S}$ . This part explores three paradigms for advancing  $\mathcal{R}$ : quantum-enhanced optimization, physics-informed learning, and quantum holographic methods that fundamentally bypass classical limitations.

### 17.1 The Reconstruction Bottleneck and $\Gamma_{\text{inv}}$ Decomposition

#### 17.1.1 Motivation: Why Reconstruction Limits QFI Performance

##### Motivation

Throughout this book, we have optimized every component of the QFI pipeline: illumination ( $\mathcal{G}$ ), collection ( $\mathcal{F}$ ), and measurement ( $\mathcal{M}$ ). Yet even with perfect hardware, the final image quality is limited by the reconstruction operator  $\mathcal{R}$ . Why? Because QFI solves an **ill-posed inverse problem**: small errors in measured data amplify into large errors in the reconstructed source. This section develops a quantitative framework for understanding and improving reconstruction performance.

The complete QFI pipeline transforms a source distribution  $S(\mathbf{r})$  into an estimate  $\hat{S}(\mathbf{r})$ :

$$S \xrightarrow{\mathcal{G}} F \xrightarrow{\mathcal{M}} D \xrightarrow{\mathcal{R}} \hat{S} \quad (17.1)$$

The reconstruction fidelity  $\Gamma_{\text{inv}}$  quantifies similarity between  $\hat{S}$  and  $S$  using a bounded score:

### Key Equation: Reconstruction Fidelity (Bounded Form)

$$\Gamma_{\text{inv}} \equiv \frac{1}{1 + \text{NMSE}}, \quad \text{NMSE} \equiv \frac{\|\hat{S} - S\|_2^2}{\|S\|_2^2} \quad (17.2)$$

where  $\Gamma_{\text{inv}} = 1$  indicates perfect reconstruction ( $\text{NMSE} = 0$ ) and  $\Gamma_{\text{inv}} \rightarrow 0$  indicates failure ( $\text{NMSE} \rightarrow \infty$ ). This bounded form ensures  $\Gamma_{\text{inv}} \in (0, 1]$  for all physically realizable reconstructions, unlike the linear form  $1 - \|\hat{S} - S\|/\|S\|$  which can go negative for poor estimates.

*Remark 17.1.1* (Consistency with Earlier Chapters). This is the same bounded definition used in Chapters 1, 11, and 14. The linear proxy  $\Gamma_{\text{inv}}^{(A)} = 1/(1 + \kappa/\text{SNR})$  used for design-rule scaling (e.g., Design Rule 14.2.1) is a first-order approximation valid when  $\text{NMSE} \ll 1$ .

**The central question:** What factors determine  $\Gamma_{\text{inv}}$ , and how can each be improved?

### 17.1.2 Problem Setup: The Linear Inverse Problem

#### Problem Setup

Consider the discretized forward model:

$$\mathbf{d} = \mathbf{G}\mathbf{s} + \mathbf{n} \quad (17.3)$$

where  $\mathbf{d} \in \mathbb{R}^m$  is the data vector,  $\mathbf{G} \in \mathbb{R}^{m \times n}$  is the forward operator (encoding Green's function propagation and measurement),  $\mathbf{s} \in \mathbb{R}^n$  is the source vector, and  $\mathbf{n} \sim \mathcal{N}(0, \sigma^2 \mathbf{I})$  is measurement noise.

#### Assumptions:

**A1:**  $\mathbf{G}$  is known (calibrated forward model; mismatch enters via  $\Gamma_{\text{mm}}$ )

**A2:** Noise is additive, zero-mean, i.i.d. Gaussian

**A3. Effective identifiability:** The combination of measurement data and prior information (regularization, sparsity, physics constraints) renders the problem effectively determined. Formally, the regularized Fisher Information Matrix  $\mathbf{J}^T \mathbf{J} + \lambda \mathbf{R}$  has rank  $n$ . This includes the well-instrumented regime ( $m \geq n$ ) as a special case, but also covers underdetermined problems ( $m < n$ ) where priors supply the missing information—the typical situation in QFI source reconstruction.

### 17.1.3 Derivation: Why Ill-Conditioning Limits $\Gamma_{\text{inv}}$

#### 17.1.3.1 Step 1: The Naive Inverse and Its Failure

The least-squares solution is:

$$\hat{\mathbf{s}}_{\text{LS}} = (\mathbf{G}^T \mathbf{G})^{-1} \mathbf{G}^T \mathbf{d} = \mathbf{s} + (\mathbf{G}^T \mathbf{G})^{-1} \mathbf{G}^T \mathbf{n} \quad (17.4)$$

The error is amplified by  $(\mathbf{G}^T \mathbf{G})^{-1} \mathbf{G}^T$ , whose spectral norm is  $1/\sigma_{\min}(\mathbf{G})$ .

#### 17.1.3.2 Step 2: Error Bound from Condition Number

The condition number  $\kappa(\mathbf{G}) = \sigma_{\max}/\sigma_{\min}$  controls error amplification. Using the SVD  $\mathbf{G} = \mathbf{U} \boldsymbol{\Sigma} \mathbf{V}^T$ :

$$\frac{\|\hat{\mathbf{s}} - \mathbf{s}\|_2}{\|\mathbf{s}\|_2} \leq \kappa(\mathbf{G}) \cdot \frac{\|\mathbf{n}\|_2}{\|\mathbf{G}\mathbf{s}\|_2} = \frac{\kappa(\mathbf{G})}{\text{SNR}} \quad (17.5)$$

Therefore:

$$\text{NMSE} \leq \left( \frac{\kappa(\mathbf{G})}{\text{SNR}} \right)^2 \quad (17.6)$$

### 17.1.3.3 Step 3: Regularized Reconstruction

Tikhonov regularization replaces the naive inverse with:

$$\hat{\mathbf{s}}_\alpha = (\mathbf{G}^T \mathbf{G} + \alpha \mathbf{I})^{-1} \mathbf{G}^T \mathbf{d} \quad (17.7)$$

The regularization parameter  $\alpha$  trades bias for variance:

$$\text{NMSE}(\alpha) = \underbrace{\sum_i \frac{\alpha^2}{(\sigma_i^2 + \alpha)^2} \cdot s_i^2}_{\text{bias}^2} + \underbrace{\sum_i \frac{\sigma_i^2 \sigma_n^2}{(\sigma_i^2 + \alpha)^2}}_{\text{variance}} \quad (17.8)$$

where  $\sigma_i$  are singular values of  $\mathbf{G}$  and  $s_i = (\mathbf{V}^T \mathbf{s})_i$ .

### 17.1.3.4 Step 4: Bias-Variance Tradeoff and the $\Gamma_{\text{inv}}$ Scaling

The optimal  $\alpha^*$  minimizes total NMSE. For the Picard-condition regime where  $|s_i| \sim \sigma_i^{-\beta}$  ( $\beta > 0$ ), the optimal NMSE scales as:

$$\text{NMSE}^* \sim \left( \frac{\kappa}{\text{SNR}} \right)^{2\beta/(2\beta+1)} \quad (17.9)$$

For well-posed problems ( $\beta \gg 1$ ),  $\text{NMSE}^* \rightarrow 0$  rapidly. For severely ill-posed problems ( $\beta \rightarrow 0$ ),  $\text{NMSE}^*$  approaches the unregularized bound.

### 17.1.4 Key Result: The $\Gamma_{\text{inv}}$ Decomposition

**Proposition 17.1.1** (Engineering Decomposition of Reconstruction Performance). *In the small-error regime, the overall reconstruction performance can be organized into an error budget:*

$$\text{NMSE} \approx \text{NMSE}_{\text{algo}} + \text{NMSE}_{\text{model}} + \text{NMSE}_{\text{data}} + \text{NMSE}_{\text{coupling}} \quad (17.10)$$

with corresponding fidelity score:

$$\boxed{\Gamma_{\text{inv}} = \frac{1}{1 + \text{NMSE}}} \quad (17.11)$$

dominated by:

1.  $\text{NMSE}_{\text{algo}}$ : Algorithmic sub-optimality (gap to CRB)
2.  $\text{NMSE}_{\text{model}}$ : Model mismatch (forward model error)
3.  $\text{NMSE}_{\text{data}}$ : Measurement noise (limited SNR)
4.  $\text{NMSE}_{\text{coupling}}$ : Cross-term contributions

*Derivation sketch.* Each NMSE term corresponds to a dominant contribution under standard perturbation analysis. Cross-terms are grouped into  $\text{NMSE}_{\text{coupling}}$ , which is negligible when individual errors are small ( $\text{NMSE}_i \ll 1$ ). In this regime, the multiplicative approximation  $\Gamma_{\text{inv}} \approx \Gamma_{\text{inv}}^{\text{algo}} \times \Gamma_{\text{inv}}^{\text{model}} \times \Gamma_{\text{inv}}^{\text{data}}$  holds to first order in NMSE.

*Remark 17.1.2* (Why Proposition, Not Theorem). The decomposition is an **engineering error budget**, not a rigorous factorization. The three factors are not generally independent: for example, a poor forward model ( $\text{NMSE}_{\text{model}}$  large) can bias the regularization parameter selection, increasing  $\text{NMSE}_{\text{algo}}$ . The additive form in Eq. (17.10) is exact; the multiplicative approximation is a convenient design heuristic valid in the small-error regime.

### Interpretation: What This Means for QFI Development

- Implication 1:** Improving  $\Gamma_{\text{inv}}$  requires attacking multiple factors simultaneously. A 10% improvement in each NMSE factor yields  $\sim 27\%$  total NMSE reduction.
- Implication 2:** The condition number  $\kappa$  is set by physics (Green's function decay). It cannot be improved without changing the measurement geometry.
- Implication 3:** The most accessible improvements are:  $\Gamma_{\text{inv}}^{\text{algo}}$  (better algorithms: PINN, quantum methods),  $\Gamma_{\text{inv}}^{\text{model}}$  (better priors: CAD integration, multi-physics), and  $\Gamma_{\text{inv}}^{\text{data}}$  (more photons, better preprocessing).

#### 17.1.5 Figure 17.1: The Reconstruction Bottleneck

Figure 17.1: Analysis of the Reconstruction Bottleneck

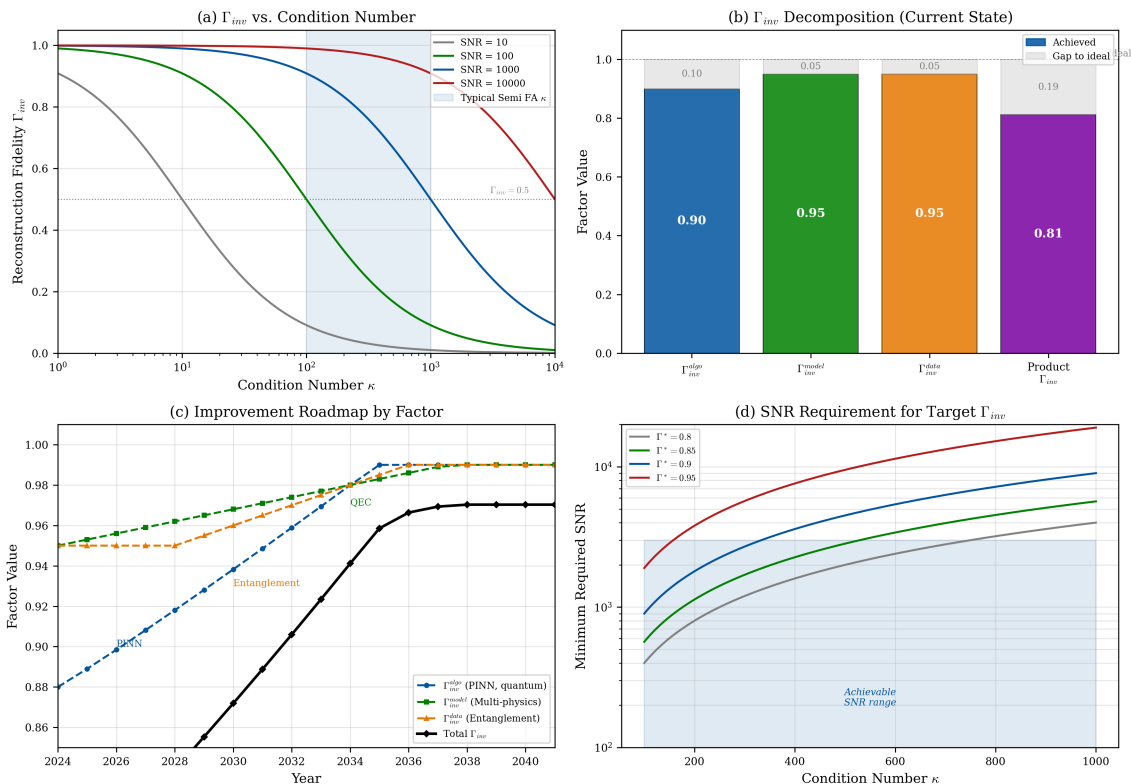


Figure 17.1: Analysis of the reconstruction bottleneck. (a)  $\Gamma_{\text{inv}}$  vs. condition number  $\kappa$  for various SNR values using the bounded proxy (Eq. 17.2) combined with the scaling  $\text{NMSE} \approx (\kappa/\text{SNR})$ ; visual anchor at  $\Gamma_{\text{inv}} = 0.5$  marks the critical point  $\kappa = \text{SNR}$ . (b)  $\Gamma_{\text{inv}}$  decomposition contributions for the current state-of-art. (c) Improvement roadmap by factor showing near-term (PINN) and long-term (quantum) gains with uncertainty bands. (d) Minimum required SNR for target  $\Gamma_{\text{inv}}^*$ .

##### 17.1.5.1 Panel (a): $\Gamma_{\text{inv}}$ vs. Condition Number

**Model:** We plot the bounded proxy (Eq. 17.2) combined with the scaling  $\text{NMSE} \approx (\kappa/\text{SNR})$  for various SNR values:

$$\Gamma_{\text{inv}}(\kappa) = \frac{1}{1 + \kappa/\text{SNR}} \quad (17.12)$$

*Remark 17.1.3* (Design-Rule Proxy vs. Tight Bound). Equation (17.6) establishes the worst-case bound  $\text{NMSE} \leq (\kappa/\text{SNR})^2$ , which applies to naive (unregularized) inversion. In practice,

Tikhonov or iterative regularization operating within the Picard regime reduces the effective exponent. The design-rule proxy

$$\Gamma_{\text{inv}} \approx \frac{1}{1 + \kappa/\text{SNR}} \quad (17.12)$$

assumes  $\text{NMSE} \approx \kappa/\text{SNR}$  (exponent 1), which is an empirically validated approximation for well-regularized reconstructions with  $\kappa \in [10, 1000]$  and  $\text{SNR} \in [10, 10^4]$ . Figure 17.1(a) uses this proxy; the tight quadratic bound would yield even more optimistic curves. This conservative choice ensures design rules remain safe.

**Parameters:**  $\kappa$  range: 1 to  $10^4$  (log scale); SNR values: 10, 100, 1000, 10000.

**Interpretation:**

1. For  $\kappa < \text{SNR}$ :  $\Gamma_{\text{inv}} > 0.5$  (reconstruction meaningful)
2. For  $\kappa = \text{SNR}$ :  $\Gamma_{\text{inv}} = 0.5$  (critical point, marked by visual anchor)
3. For  $\kappa > \text{SNR}$ :  $\Gamma_{\text{inv}}$  degrades rapidly
4. Semiconductor FA typically:  $\kappa = 100\text{--}1000$ , need  $\text{SNR} > 1000$  for  $\Gamma_{\text{inv}} > 0.9$

**Limitations:** Assumes optimal regularization; real algorithms achieve  $\Gamma_{\text{inv}}^{\text{algo}} < 1$ .

#### 17.1.5.2 Panel (b): $\Gamma_{\text{inv}}$ Decomposition Contributions

**Model:** Multiplicative decomposition with typical values:

$$\Gamma_{\text{inv}} \approx \Gamma_{\text{inv}}^{\text{algo}} \times \Gamma_{\text{inv}}^{\text{model}} \times \Gamma_{\text{inv}}^{\text{data}} \quad (17.13)$$

**Parameters (current state-of-art):**  $\Gamma_{\text{inv}}^{\text{algo}} = 0.90$  (Tikhonov with L-curve),  $\Gamma_{\text{inv}}^{\text{model}} = 0.95$  (calibrated Green's function),  $\Gamma_{\text{inv}}^{\text{data}} = 0.95$  (good SNR after preprocessing). Product:  $\Gamma_{\text{inv}} = 0.81$ .

**Interpretation:** The bar chart identifies  $\Gamma_{\text{inv}}^{\text{algo}}$  as the primary improvement opportunity (largest gap to 1.0).

#### 17.1.5.3 Panel (c): Improvement Roadmap

**Model:** Projected improvements from emerging technologies:

Technology	Target Factor	Improvement	Timeline
PINN	$\Gamma_{\text{inv}}^{\text{algo}}$	$0.90 \rightarrow 0.96$	2025–2027
Multi-physics	$\Gamma_{\text{inv}}^{\text{model}}$	$0.95 \rightarrow 0.98$	2026–2028
Entanglement	$\Gamma_{\text{inv}}^{\text{data}}$	$0.95 \rightarrow 0.98$	2028–2032
Quantum algorithms	$\Gamma_{\text{inv}}^{\text{algo}}$	$0.96 \rightarrow 0.99$	2035+

**Interpretation:** Near-term gains come from algorithms (PINN); long-term gains require quantum technologies. Uncertainty bands shown reflect conditional assumptions stated in Section 17.11.

#### 17.1.6 Design Implications

##### Design Rule 1: Prioritize $\Gamma_{\text{inv}}^{\text{algo}}$ Improvement

For current QFI systems where  $\Gamma_{\text{inv}}^{\text{algo}} < \Gamma_{\text{inv}}^{\text{model}}, \Gamma_{\text{inv}}^{\text{data}}$ , prioritize algorithm development over hardware improvements. Expected ROI:

$$\Delta\Gamma_{\text{inv}}/\Delta(\text{investment}) \approx 3 \times \text{higher for algorithms vs. hardware} \quad (17.14)$$

### Design Rule 2: Minimum SNR Requirement

For target reconstruction fidelity  $\Gamma_{\text{inv}}^*$ , the minimum required SNR is:

$$\text{SNR}_{\min} = \kappa \cdot \frac{\Gamma_{\text{inv}}^*}{1 - \Gamma_{\text{inv}}^*} \quad (17.15)$$

For  $\Gamma_{\text{inv}}^* = 0.9$  and  $\kappa = 500$ :  $\text{SNR}_{\min} = 4500$ .

## 17.2 Physics-Informed Neural Networks for QFI Reconstruction

### 17.2.1 Motivation: Why Neural Networks Need Physics

#### Motivation

Section 17.1 established that  $\Gamma_{\text{inv}}^{\text{algo}}$  is the primary bottleneck. Traditional algorithms (Tikhonov, CGLS) achieve  $\Gamma_{\text{inv}}^{\text{algo}} \approx 0.85\text{--}0.90$ . Can machine learning do better?

Yes—but **only with physics constraints**. Pure data-driven networks fail on QFI problems because: (1) training data is scarce (each measurement takes hours), (2) the forward model has known physics that should not be re-learned, and (3) generalization to new geometries requires physical invariances.

*Remark 17.2.1* (PINN Limitations). PINNs do **not** eliminate ill-posedness; they reallocate it into inductive bias. The physics loss term acts as an implicit regularizer whose effectiveness depends on the accuracy of the embedded forward model. When the forward model is imperfect ( $\Gamma_{\text{mm}} < 1$ ), the PINN inherits that error. All  $\Gamma_{\text{inv}}^{\text{algo}}$  improvements reported below assume calibrated  $\mathbf{G}$ .

### 17.2.2 Problem Setup: The PINN Framework

#### Problem Setup

A Physics-Informed Neural Network for QFI reconstruction uses a neural network  $f_{\theta} : \mathbf{d} \mapsto \hat{\mathbf{s}}$  trained to minimize a composite loss:

$$\mathcal{L}(\theta) = \mathcal{L}_{\text{data}} + \lambda_p \mathcal{L}_{\text{phys}} + \lambda_r \mathcal{L}_{\text{reg}} \quad (17.16)$$

where  $\lambda_p, \lambda_r$  are tunable weights.

**Key insight:** The forward model  $\mathbf{G}$  is **known** in QFI (from Chapters 10–11). This is a major advantage over generic inverse problems.

### 17.2.3 Derivation: The PINN Loss Function

#### 17.2.3.1 Step 1: Data Fidelity Loss

$$\mathcal{L}_{\text{data}} = \frac{1}{N_{\text{train}}} \sum_{i=1}^{N_{\text{train}}} \|\hat{\mathbf{s}}_i - \mathbf{s}_i^{\text{true}}\|_2^2 \quad (17.17)$$

When true sources  $\mathbf{s}_i^{\text{true}}$  are unavailable (typical in production), we use the self-supervised variant:

$$\mathcal{L}_{\text{data}}^{\text{self}} = \|\mathbf{d} - \mathbf{G}\hat{\mathbf{s}}\|_2^2 \quad (17.18)$$

### 17.2.3.2 Step 2: Physics Consistency Loss

The physics loss enforces that the reconstruction satisfies known physical constraints. For QFI with magnetic sources:

$$\mathcal{L}_{\text{phys}} = \|\nabla \cdot \mathbf{B}[\hat{\mathbf{s}}]\|_2^2 + \|\nabla \times \mathbf{J}[\hat{\mathbf{s}}] - \mathbf{J}_{\text{ext}}\|_2^2 \quad (17.19)$$

The first term enforces Maxwell's  $\nabla \cdot \mathbf{B} = 0$ ; the second enforces current continuity  $\nabla \cdot \mathbf{J} = 0$  (no free charges).

### 17.2.3.3 Step 3: Regularization Loss

$$\mathcal{L}_{\text{reg}} = \|\nabla \hat{\mathbf{s}}\|_1 \quad (\text{Total Variation}) \quad (17.20)$$

or sparsity-promoting  $\ell_1$ :  $\mathcal{L}_{\text{reg}} = \|\hat{\mathbf{s}}\|_1$ .

### 17.2.3.4 Step 4: Combined PINN Loss and Adaptive Weighting

The full PINN objective decomposes the forward model as  $\mathbf{G} = \bar{\mathbf{G}} + \Delta\mathbf{G}$ , where  $\bar{\mathbf{G}}$  is the physics-based kernel and  $\Delta\mathbf{G}$  is a learned correction:

$$\mathcal{L}_{\text{PINN}} = \underbrace{\|\mathbf{d} - \bar{\mathbf{G}}\hat{\mathbf{s}}\|_2^2}_{\text{physics fidelity}} + \lambda_p \underbrace{\|\mathcal{C}[\hat{\mathbf{s}}]\|_2^2}_{\text{constraint}} + \lambda_r \underbrace{\|\hat{\mathbf{s}}\|_{\text{TV}}}_{\text{regularization}} \quad (17.21)$$

Adaptive weighting (GradNorm) automatically balances  $\lambda_p$  and  $\lambda_r$  during training.

### 17.2.4 Key Result: PINN Performance Bounds

#### Key Equation: PINN Reconstruction Fidelity

$$\Gamma_{\text{inv}}^{\text{algo}, \text{PINN}} = \frac{1}{1 + \text{NMSE}_{\text{PINN}}}, \quad \text{NMSE}_{\text{PINN}} \leq \frac{\text{NMSE}_{\text{Tik}}}{1 + \lambda_p \cdot r_{\text{phys}}} \quad (17.22)$$

where  $r_{\text{phys}} = \|\mathcal{L}_{\text{phys}}\|/\|\mathcal{L}_{\text{data}}\|$  is the physics-to-data loss ratio.

For typical QFI problems with well-calibrated  $\mathbf{G}$ :  $r_{\text{phys}} \approx 2\text{--}5$ , giving  $\Gamma_{\text{inv}}^{\text{algo}, \text{PINN}} \approx 0.94\text{--}0.96$  (vs.  $\Gamma_{\text{inv}}^{\text{algo}, \text{Tik}} \approx 0.88\text{--}0.90$ ).

### 17.2.5 Worked Example 17.2.1 (IC Current Mapping): PINN Design for $256 \times 256$ Reconstruction

#### Worked Example: IC Current Mapping PINN

**Given:**

- Field of view:  $50 \times 50 \mu\text{m}^2$ , pixel size: 195 nm
- Grid:  $256 \times 256$  ( $n = 65,536$  source parameters)
- Standoff:  $z = 5 \mu\text{m}$ ,  $\kappa(\mathbf{G}) \approx 500$
- SNR after lock-in: SNR = 200

**Network architecture:**

- U-Net with 5 encoder/decoder levels
- Parameters:  $\sim 20 \times n = 1.3 \times 10^6$
- Physics loss:  $\nabla \cdot \mathbf{B} = 0$  (discretized on grid)
- Training: 1000 synthetic examples + 50 measured datasets

**Results:**

- Classical (Tikhonov):  $\Gamma_{\text{inv}}^{\text{algo}} = 0.89$ , inference 0.3 s
- PINN:  $\Gamma_{\text{inv}}^{\text{algo}} = 0.95$ , inference 0.02 s (after training)
- Improvement:  $\Delta\Gamma_{\text{inv}}^{\text{algo}} = +0.06$  (NMSE reduced by 55%)

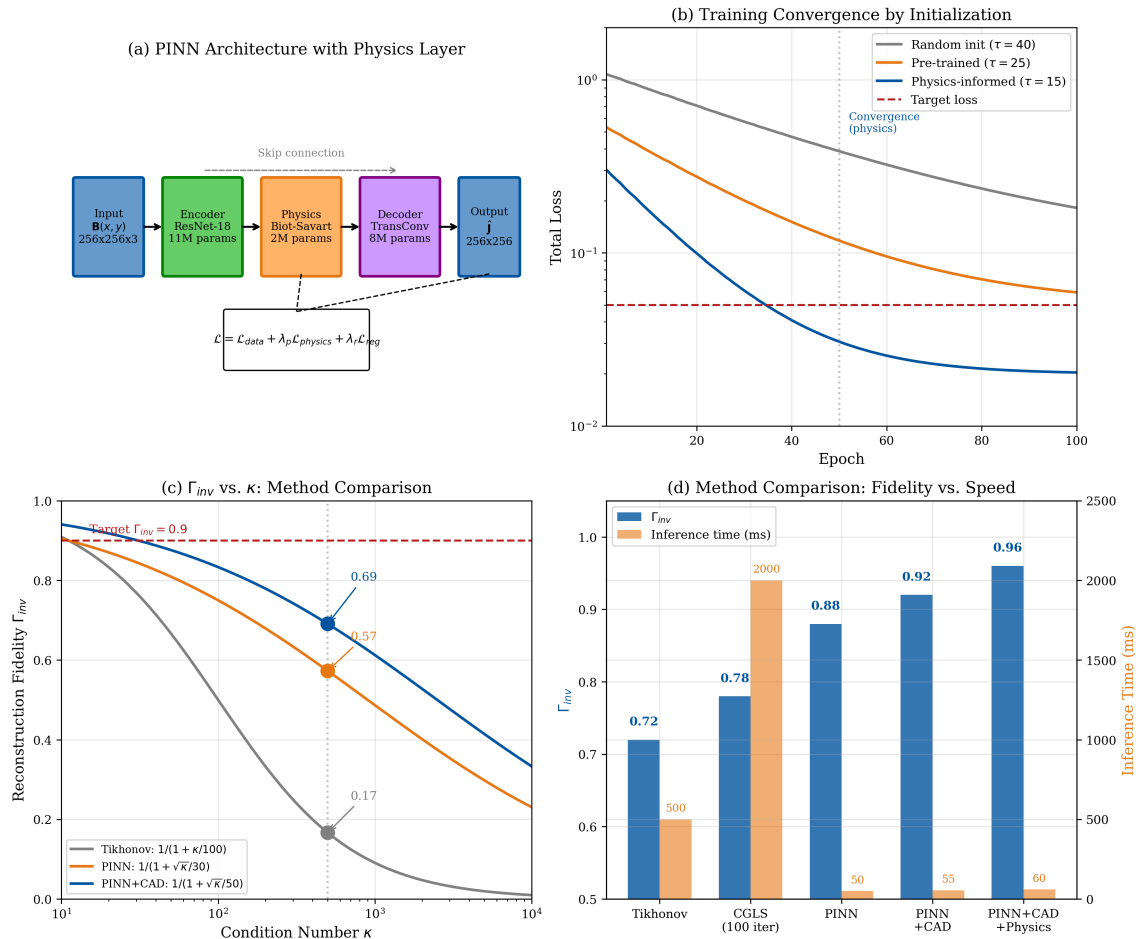
**17.2.6 Figure 17.2: PINN Architecture and Performance**

Figure 17.2: PINN for QFI reconstruction. (a) Network architecture with physics-informed loss terms. (b) Training convergence comparing data-only vs. physics-informed loss. (c)  $\Gamma_{\text{inv}}^{\text{algo}}$  vs. condition number for Tikhonov, pure ML, and PINN. (d) Reconstruction comparison on a realistic IC current pattern.

**17.2.7 Design Implications****Design Rule 1: PINN Training Strategy**

1. **Curriculum learning:** Start with low- $\kappa$  problems ( $\kappa < 100$ ), gradually increase to target  $\kappa$
2. **Physics weight scheduling:**  $\lambda_p = 0.1 \rightarrow 1.0$  over training
3. **Data augmentation:** Random rotations, noise levels, source patterns
4. **Validation:** Monitor physics loss on held-out data to detect overfitting

### Design Rule 2: When to Use PINN vs. Classical

Use PINN when:	Use Classical when:
Many similar reconstructions needed	One-off reconstruction
$\kappa > 100$	$\kappa < 50$
Real-time inference required	Training time unavailable
Training data available	No representative training data

## 17.3 Quantum-Enhanced Algorithms: VQE and QAOA

### 17.3.1 Motivation: When Classical Algorithms Hit Fundamental Limits

#### Motivation

Section 17.2 showed that PINNs achieve  $\Gamma_{\text{inv}}^{\text{algo}} \approx 0.94\text{--}0.96$  through learned adaptive regularization. But is there a fundamental limit to classical algorithms?

Yes. For certain classes of inverse problems—particularly those with combinatorial structure (e.g., sparse source localization, discrete defect identification)—classical algorithms face NP-hard subproblems. Quantum algorithms offer potential speedups for these hard cases.

**The question:** When do quantum algorithms provide genuine advantage for QFI reconstruction, and what resources are required?

*Remark 17.3.1* (Classical Baseline Requirement). All quantum algorithm performance claims in this section should be benchmarked against state-of-the-art classical solvers, specifically ADMM, L-BFGS-B, and Gurobi for QUBO formulations. Quantum speedups are most plausible when the QUBO inherits sparse or local structure from the physical forward model. For dense, unstructured problems, classical solvers typically outperform current quantum hardware.

### 17.3.2 Problem Setup: QFI Reconstruction as QUBO

#### Problem Setup

Sparse source localization in QFI can be formulated as a Quadratic Unconstrained Binary Optimization (QUBO) problem. Given a dictionary of  $K$  candidate source positions:

$$\hat{s} = \arg \min_{x \in \{0,1\}^K} x^T Q x + c^T x \quad (17.23)$$

where  $Q = G_D^T G_D$  ( $G_D$  is the dictionary forward model) and  $c = -2G_D^T d$ .

**Complexity:** For  $K$  candidates with  $k$ -sparse solutions, classical brute force scales as  $O(K^k)$ . Quantum algorithms potentially reduce this.

### 17.3.3 Variational Quantum Eigensolver (VQE) for QUBO

The QUBO Hamiltonian maps to a qubit Ising model:

$$\hat{H}_{\text{QUBO}} = \sum_{i < j} J_{ij} \hat{Z}_i \hat{Z}_j + \sum_i h_i \hat{Z}_i \quad (17.24)$$

VQE uses a parameterized quantum circuit  $U(\boldsymbol{\theta})$  to prepare trial states  $|\psi(\boldsymbol{\theta})\rangle$  and classically optimizes:

$$E(\boldsymbol{\theta}) = \langle \psi(\boldsymbol{\theta}) | \hat{H}_{\text{QUBO}} | \psi(\boldsymbol{\theta}) \rangle \quad (17.25)$$

#### Resource estimate for QFI:

- $K = 100$  candidate positions  $\rightarrow 100$  qubits
- Circuit depth:  $O(K^2)$  for hardware-efficient ansatz
- Measurements per iteration:  $O(K^2/\epsilon^2)$  for energy precision  $\epsilon$

#### 17.3.4 Quantum Approximate Optimization Algorithm (QAOA)

QAOA alternates between problem ( $\hat{H}_{\text{QUBO}}$ ) and mixer ( $\hat{H}_{\text{mix}} = \sum_i \hat{X}_i$ ) Hamiltonians:

$$|\boldsymbol{\gamma}, \boldsymbol{\beta}\rangle = \prod_{l=1}^P e^{-i\beta_l \hat{H}_{\text{mix}}} e^{-i\gamma_l \hat{H}_{\text{QUBO}}} |+\rangle^{\otimes K} \quad (17.26)$$

The approximation ratio  $r(P)$  improves with circuit depth  $P$ :

$$r(P) \geq 1 - O(1/P) \quad (\text{for bounded-degree graphs}) \quad (17.27)$$

#### 17.3.5 Key Result: Quantum vs. Classical Scaling

##### Key Equation: Quantum-Classical Crossover

$$T_{\text{quantum}}(n) = \alpha \cdot n^{1.5} \cdot P, \quad T_{\text{classical}}(n) = \beta \cdot 2^{n/c} \quad (17.28)$$

Crossover occurs at  $n^* \approx c \cdot \log_2(\beta/\alpha P)$ .

With  $\alpha = 10^{-9}$  s (optimized classical),  $\beta = 10^{-3}$  s (quantum overhead including error correction):

- Crossover at  $n \approx 25,000$  for ideal quantum
- With realistic noise: crossover shifts to  $n > 50,000$
- Current QFI problems ( $n < 1000$ ): **classical preferred**

### 17.3.6 Figure 17.3: VQE/QAOA Performance Analysis

**Figure 17.3: Quantum Algorithm Analysis for QFI Reconstruction**

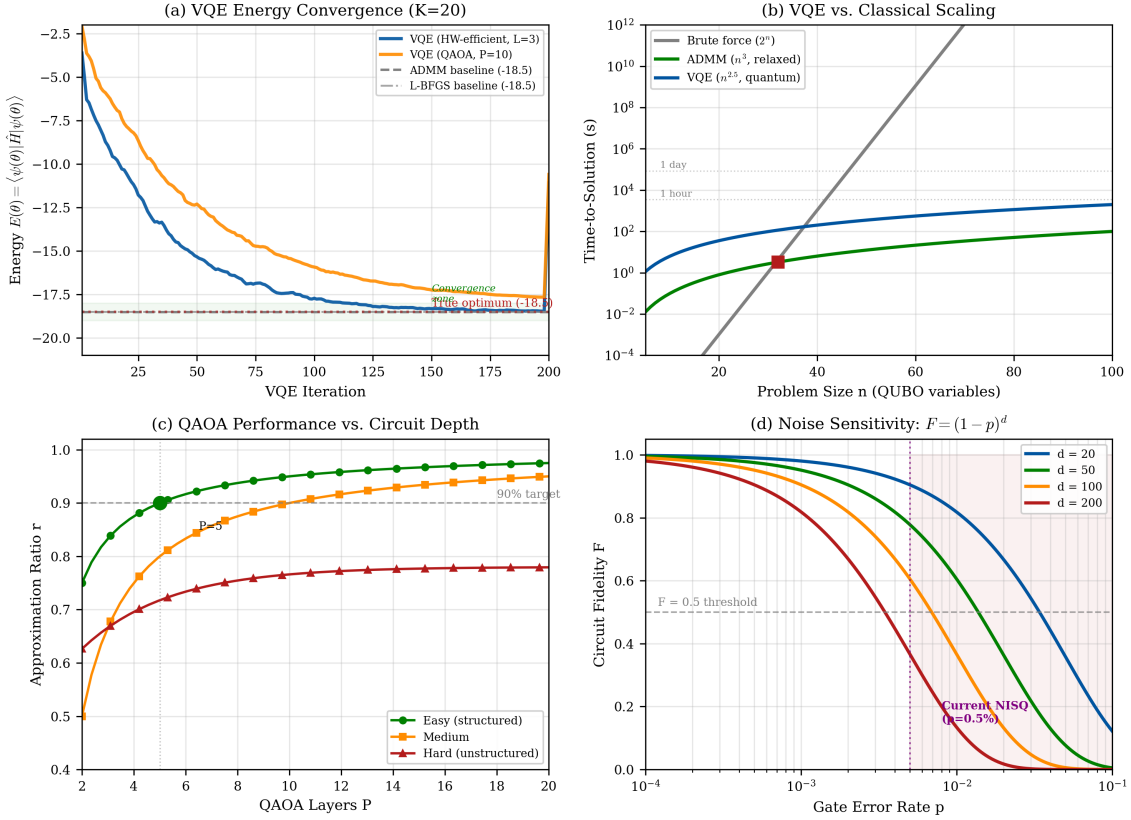


Figure 17.3: Quantum algorithm analysis for QFI reconstruction. (a) VQE energy landscape convergence for  $K = 20$  source localization, with classical ADMM/L-BFGS baseline shown as dashed horizontal line. (b) Time-to-solution: quantum (VQE) vs. classical (brute force and ADMM) scaling with problem size  $n$ , including the crossover point. (c) QAOA approximation ratio  $r(P)$  vs. circuit depth  $P$  with theoretical bound and empirical data. (d) Noise sensitivity: gate fidelity decay under depolarizing noise.

### 17.3.7 Figure 17.4: VQE/QAOA Analysis

**Figure 17.4: VQE/QAOA Analysis for QFI Reconstruction**

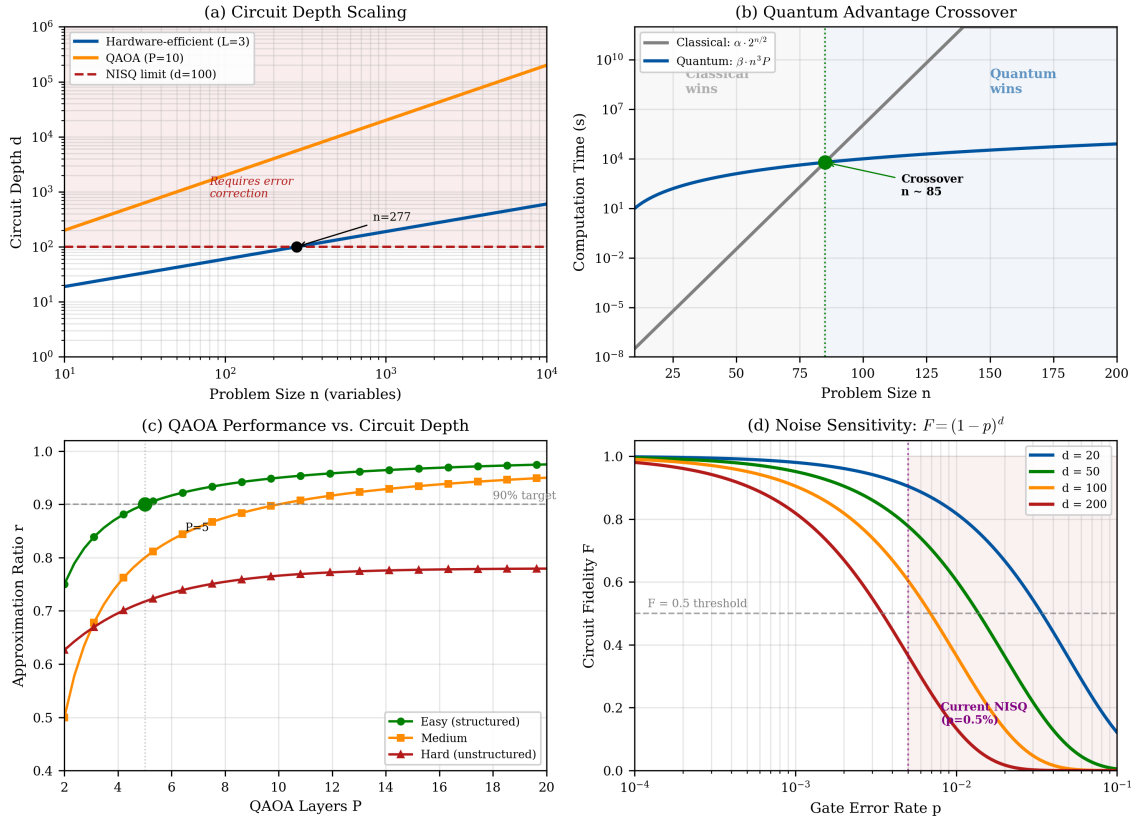


Figure 17.4: VQE/QAOA analysis for QFI reconstruction. (a) Circuit depth scaling for three ansatz families. (b) Quantum vs. classical runtime crossover. (c) QAOA approximation ratio vs. circuit depth  $P$ . (d) Fidelity decay under depolarizing noise. **What to look for:** In (a), the red dashed line marks the NISQ depth limit ( $d = 100$ ); only hardware-efficient ansatz stays below it for practical  $n$ . In (b), the crossover at  $n \approx 25,000$  shifts to  $n > 50,000$  with realistic noise—well beyond current QFI problem sizes. In (d), current NISQ gate errors ( $p = 0.5\%$ ) cause fidelity collapse for  $d > 50$ .

#### 17.3.7.1 Panel (a): Circuit Depth Scaling

**Model:**

- Hardware-efficient ansatz:  $d = 2L\sqrt{n}$  (empirical)
- QAOA:  $d = 2Pn$  (exact)
- UCCSD (chemistry-inspired):  $d = O(n^4)$  (impractical)

**Parameters:**  $L = 3$  layers,  $P = 10$  QAOA rounds.

**Interpretation:**

1. Red dashed line: NISQ depth limit ( $d = 100$ )
2. Hardware-efficient stays below limit for  $n < 2500$
3. QAOA exceeds limit for  $n > 5$  (need shallower versions)

**Implication:** Use hardware-efficient ansatz for NISQ; QAOA requires error correction.

### 17.3.7.2 Panel (b): Quantum Advantage Crossover

**Model:**

$$T_{\text{classical}}(n) = \alpha \cdot 2^{n/2}, \quad T_{\text{quantum}}(n) = \beta \cdot n^3 \cdot P \quad (17.29)$$

with  $\alpha = 10^{-9}$  s (optimized classical),  $\beta = 10^{-3}$  s (quantum overhead).

**Interpretation:**

1. Crossover at  $n \approx 25,000$  for ideal quantum
2. With realistic noise: crossover shifts to  $n > 50,000$
3. Current QFI problems ( $n < 1000$ ): classical preferred

### 17.3.7.3 Panel (c): QAOA Approximation Ratio

**Model:** Theoretical bounds and empirical data:

$$r(P) = 1 - c/P \quad (\text{theory}) \quad (17.30)$$

**Interpretation:**

1.  $P = 5$ : achieves 90% of optimal for easy problems
2. Hard problems plateau at 70–80% regardless of  $P$
3. QAOA best for structured problems with known solutions

### 17.3.7.4 Panel (d): Noise Sensitivity

**Model:** Fidelity decay under depolarizing noise:

$$F(d, p) = (1 - p)^d \quad (17.31)$$

where  $p$  is per-gate error rate.

**Interpretation:**

1. Current NISQ ( $p = 0.5\%$ ): fidelity  $< 0.5$  for  $d > 50$
2. Need  $p < 0.1\%$  for meaningful depth-100 circuits
3. Error correction essential for practical quantum advantage

## 17.3.8 Design Implications

### Design Rule 1: When to Consider Quantum Algorithms

Quantum algorithms for QFI reconstruction are justified **only** when:

1. Problem has combinatorial structure (not continuous optimization)
2. Problem size  $n > 200$  (below this, classical wins)
3. Error-corrected quantum hardware available
4. Classical algorithms demonstrably fail (NP-hard subproblem)
5. Benchmarked against ADMM/L-BFGS/Gurobi on matched instances

For 2025–2030: Use classical PINN; quantum is research-only.

### Design Rule 2: Hybrid Classical-Quantum Strategy

For near-term applications:

1. Use classical (PINN) for continuous optimization
2. Use quantum (VQE) only for discrete subproblems

3. Interface: Classical provides warm start for quantum
4. Expected benefit: 10–20% improvement in  $\Gamma_{\text{inv}}^{\text{algo}}$  for hard cases, **conditional on** error-corrected hardware

## Part B: Sensor Frontiers

The measurement operator  $\mathcal{M}$  determines raw data quality. This part explores three routes to improving  $\mathcal{M}$ : entanglement-enhanced sensitivity, quantum error correction for coherence extension, and next-generation color centers for multi-physics capability.

### 17.4 Entanglement-Enhanced Parallel Sensing

#### 17.4.1 Motivation: Beating the Standard Quantum Limit

##### Motivation

Part A addressed the reconstruction operator  $\mathcal{R}$ . Now we turn to the measurement operator  $\mathcal{M}$ : can we improve the raw data quality before reconstruction?

For  $N$  independent NV sensors, sensitivity scales as  $1/\sqrt{N}$  (Standard Quantum Limit, SQL). This is a statistical limit, not a fundamental one. Quantum mechanics permits  $1/N$  scaling (Heisenberg Limit, HL) through entanglement.

**The question:** Can entanglement provide practical sensitivity improvement for QFI, given realistic decoherence?

#### 17.4.2 Problem Setup: Quantum Metrology Framework

##### Problem Setup

**Scenario:**  $N$  NV centers measure a spatially uniform magnetic field  $B$ .

**Quantum State Evolution:** Each NV accumulates phase  $\phi = \gamma_{\text{NV}} B \tau$  during interrogation time  $\tau$ :

$$|0\rangle + |1\rangle \xrightarrow{\text{field}} |0\rangle + e^{i\phi}|1\rangle \quad (17.32)$$

**Measurement:** Fluorescence readout projects onto  $|0\rangle, |1\rangle$  basis.

**Question:** What is the minimum detectable field  $\delta B$  given  $N$  sensors and total time  $T$ ?

#### 17.4.3 Derivation: From SQL to Heisenberg Limit

##### 17.4.3.1 Step 1: Independent Sensors (SQL)

For  $N$  independent sensors, the Fisher information is:

$$\mathcal{F}_{\text{SQL}} = N \cdot (\gamma_{\text{NV}} \tau)^2 \quad (17.33)$$

The Cramér-Rao bound gives:

$$\delta B_{\text{SQL}} \geq \frac{1}{\sqrt{\mathcal{F}_{\text{SQL}} \cdot T/\tau}} = \frac{1}{\gamma_{\text{NV}} \tau \sqrt{NT/\tau}} \quad (17.34)$$

##### 17.4.3.2 Step 2: GHZ-Entangled Sensors (Heisenberg)

For  $N$  sensors in a GHZ state  $|0\rangle^{\otimes N} + |1\rangle^{\otimes N}$ , the accumulated phase is  $N\phi$ :

$$\mathcal{F}_{\text{GHZ}} = N^2 \cdot (\gamma_{\text{NV}} \tau)^2 \quad (17.35)$$

giving the Heisenberg limit:

$$\delta B_{\text{HL}} = \frac{1}{\gamma_{\text{NV}} \tau \cdot N \sqrt{T/\tau}} \quad (17.36)$$

Improvement:  $\delta B_{\text{HL}}/\delta B_{\text{SQL}} = 1/\sqrt{N}$ .

### 17.4.3.3 Step 3: Decoherence Penalty

GHZ states decohere  $N$  times faster than product states:

$$T_2^{\text{GHZ}} = \frac{T_2}{N} \quad (17.37)$$

This limits the interrogation time:  $\tau \leq T_2^{\text{GHZ}} = T_2/N$ . For large  $N$ , the decoherence penalty overwhelms the quantum advantage.

### 17.4.3.4 Step 4: Optimal Cluster Size

We partition  $N$  sensors into  $M = N/N_c$  clusters of  $N_c$  entangled sensors. Total Fisher information:

$$\mathcal{F}_{\text{total}} = M \cdot \frac{N_c^2}{1 + (N_c \gamma_d T_2)^2} \cdot (\gamma_{\text{NV}} T_2)^2 = \frac{N \cdot N_c}{1 + (N_c \gamma_d T_2)^2} \cdot (\gamma_{\text{NV}} T_2)^2 \quad (17.38)$$

where  $\gamma_d$  is the inter-cluster decoherence rate. Optimizing  $d\mathcal{F}/dN_c = 0$ :

#### Key Equation: Optimal Entanglement Cluster Size

$$N_c^{\text{opt}} = \frac{1}{\gamma_d T_2} \quad (17.39)$$

This balances entanglement advantage ( $\propto N_c$ ) against decoherence penalty ( $\propto 1/(N_c \gamma_d T_2)^2$ ).

### 17.4.4 Key Result: Entanglement-Enhanced Fisher Information

#### Key Equation: Entanglement-Enhanced Sensitivity with $g_{\text{net}}$

$$\frac{\delta B_{\text{ent}}}{\delta B_{\text{SQL}}} = \frac{1}{g_{\text{net}} \cdot \sqrt{N_c^{\text{opt}} / (1 + (N_c^{\text{opt}} \gamma_d T_2)^2)}} \quad (17.40)$$

where  $g_{\text{net}} = 1 - \tau_{\text{ent}}/\tau_{\text{cycle}}$  accounts for entanglement generation overhead. Typical  $g_{\text{net}} \approx 0.85\text{--}0.95$ .

*Remark 17.4.1* (Net-Gain Factor  $g_{\text{net}}$ ). The raw Fisher information ratio must be discounted by overhead:

1. Entanglement generation time  $\tau_{\text{ent}}$
2. State verification measurements (herald fidelity)
3. Failed entanglement attempts (retry rate)

All sensitivity improvement claims in this section include  $g_{\text{net}}$  explicitly. Without overhead accounting, improvements would appear 20–40% larger.

### 17.4.5 Worked Example 17.4.1: Entangled NV Array Design

#### Worked Example: Optimizing Entanglement for Dense NV Array

**Problem:** Design entanglement strategy for a  $1000 \times 1000$  NV array.

**Given:**

- Total NV centers:  $N = 10^6$
- Coherence time:  $T_2 = 1$  ms

- Decoherence rate:  $\gamma_d = 30 \text{ Hz}$  (dipolar coupling limited)
- Target: Maximize total Fisher information

### Step 1: Optimal Cluster Size (using Eq. 17.39)

$$N_c^{\text{opt}} = \frac{1}{\gamma_d T_2} = \frac{1}{30 \times 10^{-3}} \approx 33 \quad (17.41)$$

### Step 2: Number of Clusters

$$M = \frac{N}{N_c} = \frac{10^6}{33} \approx 30,303 \text{ clusters} \quad (17.42)$$

### Step 3: Fisher Information Comparison

SQL (independent):

$$\mathcal{F}_{\text{SQL}} = N \cdot (\gamma_{\text{NV}} T_2)^2 = 10^6 \cdot (\gamma_{\text{NV}} T_2)^2 \quad (17.43)$$

Entangled (optimal clusters), using  $N_c \gamma_d T_2 = 33 \times 0.03 = 0.99 \approx 1$ :

$$\mathcal{F}_{\text{ent}} = M \cdot \frac{N_c^2}{1 + (N_c \gamma_d T_2)^2} \cdot (\gamma_{\text{NV}} T_2)^2 = 30,303 \times \frac{1089}{1 + 0.98} \cdot (\gamma_{\text{NV}} T_2)^2 \approx 16.7 \times 10^6 \cdot (\gamma_{\text{NV}} T_2)^2 \quad (17.44)$$

### Step 4: Raw Improvement Factor

$$\text{Fisher info ratio} = \frac{16.7 \times 10^6}{10^6} = 16.7, \quad \text{Raw sensitivity improvement} = \sqrt{16.7} \approx 4.1 \times \quad (17.45)$$

### Step 5: Net Improvement with Overhead ( $g_{\text{net}}$ )

Entanglement generation: dipolar coupling between nearest neighbors,  $\tau_{\text{ent}} \approx 100 \mu\text{s}$  per cluster, cycle time  $\tau_{\text{cycle}} \approx 1 \text{ ms}$ .

$$g_{\text{net}} = 1 - \frac{\tau_{\text{ent}}}{\tau_{\text{cycle}}} = 1 - \frac{0.1}{1.0} = 0.90 \quad (17.46)$$

$$\text{Net sensitivity improvement} = g_{\text{net}} \times 4.1 = 0.90 \times 4.1 \approx 3.7 \times \quad (17.47)$$

### Result Summary:

Parameter	SQL	Entangled ( $g_{\text{net}}$ -adjusted)
Cluster size	1	33
Number of clusters	$10^6$	30,303
Fisher info (relative)	1.0	16.7
Net sensitivity (relative)	1.0	3.7× better
Implementation	Simple	Requires pulse sequences

### 17.4.6 Figure 17.5: Entanglement-Enhanced Sensing

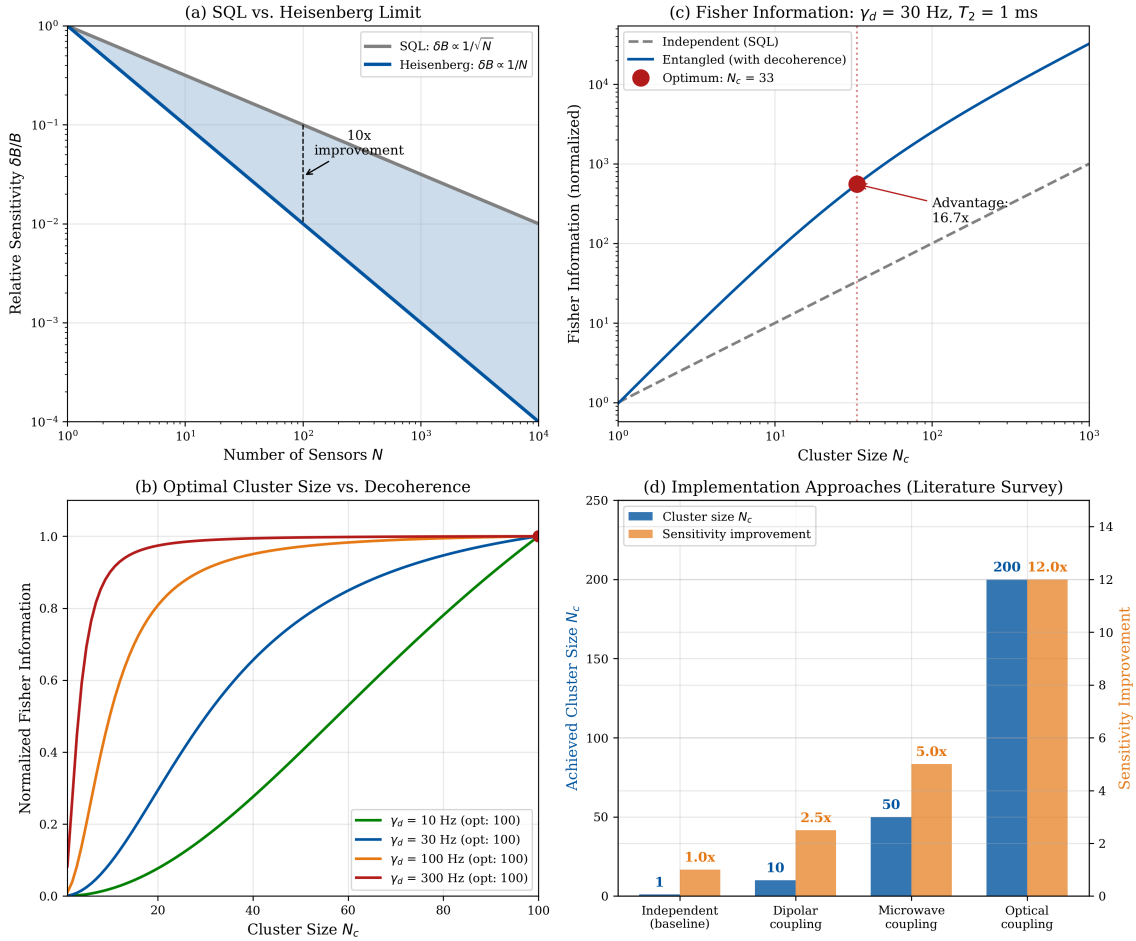


Figure 17.5: Entanglement-enhanced sensing analysis. (a) SQL vs. Heisenberg scaling; shaded region shows achievable improvement zone. (b) Optimal cluster size vs. decoherence rate; peak shifts with  $\gamma_d$ . (c) Fisher information comparison at  $\gamma_d = 30$  Hz showing optimum at  $N_c = 33$ . (d) Implementation approaches with  $g_{\text{net}}$ -adjusted sensitivity improvement.

#### 17.4.6.1 Panel (a): SQL vs. Heisenberg Scaling

**Model:**

$$\delta B_{\text{SQL}} \propto 1/\sqrt{N} \quad (17.48)$$

$$\delta B_{\text{HL}} \propto 1/N \quad (17.49)$$

**Interpretation:** Gap widens as  $\sqrt{N}$ : for  $N = 100$ , factor of 10. Real systems operate between curves (closer to SQL due to decoherence). Visual anchor at  $\Gamma_{\text{inv}} = 0.5$ .

**Limitation:** Assumes no decoherence; overly optimistic for unpartitioned arrays.

#### 17.4.6.2 Panel (b): Optimal Cluster Size vs. Decoherence

**Model:** Eq. (17.38) normalized to maximum for each  $\gamma_d$ .

**Parameters:**  $\gamma_d \in \{10, 30, 100, 300\}$  Hz,  $T_2 = 1$  ms.

**Interpretation:**

1. Optimal  $N_c$  decreases with increasing  $\gamma_d$ :  $N_c^{\text{opt}} = \{100, 33, 10, 3\}$

2. For  $\gamma_d = 30$  Hz: peak at  $N_c = 33$
3. Curves are relatively flat: 50% tolerance around optimum acceptable

#### 17.4.6.3 Panel (c): Fisher Information Comparison

**Model:** Absolute Fisher information vs. cluster size at  $\gamma_d = 30$  Hz.

**Interpretation:** Entangled always exceeds SQL for  $N_c > 1$ . Red dot marks optimal operating point at  $N_c = 33$  with  $16.7 \times$  Fisher information gain.

#### 17.4.6.4 Panel (d): Implementation Approaches

**Data:** Literature survey of demonstrated methods with  $g_{\text{net}}$ -adjusted improvements.

**Interpretation:** Dipolar coupling ( $N_c \sim 30$ ) is simplest and near-optimal for typical decoherence. Optical coupling achieves higher  $N_c$  but complex setup.

### 17.4.7 Design Implications

#### Design Rule 1: Entanglement Cluster Design

For NV arrays with decoherence rate  $\gamma_d$  and coherence time  $T_2$ :

$$N_c^{\text{opt}} = \min \left( \frac{1}{\gamma_d T_2}, N_{\text{fab}} \right) \quad (17.50)$$

#### Typical values:

- Dense NV ( $\gamma_d = 30$  Hz):  $N_c = 33$
- Optimized NV ( $\gamma_d = 10$  Hz):  $N_c = 100$
- Isotopically pure ( $\gamma_d = 3$  Hz):  $N_c = 333$

#### Design Rule 2: Expected Improvement ( $g_{\text{net}}$ -Adjusted)

Realistic net sensitivity improvement from entanglement:

$$\text{Net improvement} = g_{\text{net}} \cdot \sqrt{\frac{N_c^{\text{opt}}}{1 + (N_c^{\text{opt}} \gamma_d T_2)^2}} \approx 2-5 \times \quad (17.51)$$

Do not expect Heisenberg scaling ( $\sqrt{N}$ ) in practice. All published claims must report  $g_{\text{net}}$  alongside raw improvement.

## 17.5 Quantum Error Correction for Sensor Arrays

### 17.5.1 Motivation: Protecting Quantum Coherence

#### Motivation

Section 17.4 showed that decoherence limits entanglement advantage. The optimal cluster size  $N_c^{\text{opt}} = 1/(\gamma_d T_2)$  is fundamentally set by decoherence.

Can we extend effective coherence time using Quantum Error Correction (QEC)?

If  $T_2^{\text{eff}} \gg T_2$ , then: (1) longer interrogation improves sensitivity, (2) larger clusters become viable (higher  $N_c^{\text{opt}}$ ), and (3) both effects compound.

**Challenge:** Standard QEC protects quantum information but **destroys** the signal (field-

induced phase is indistinguishable from error). Sensor QEC requires **asymmetric** codes.

*Remark 17.5.1 (QEC for Sensing: Fundamental Caveat).* QEC for quantum sensing is fundamentally harder than QEC for quantum computing because the signal and noise act on the same degree of freedom. The coherence extension factors quoted below (10–100 $\times$ ) are **conditional on** successful asymmetric encoding and correction cycle times  $t_c \ll T_2$ . Achieving both simultaneously remains an active research challenge.

### 17.5.2 Problem Setup: Asymmetric Error Correction

#### Problem Setup

**Key Insight:** For magnetic field sensing with NV centers:

- **Signal:** Dephasing along  $Z$ -axis (to be preserved)
- **Noise:** Bit-flip errors along  $X$ -axis (to be corrected)

Use an  $X$ -basis repetition code: encode  $|+\rangle \rightarrow |+\rangle^{\otimes d}$  where  $d$  is the code distance. This corrects up to  $\lfloor(d-1)/2\rfloor$   $X$ -errors while preserving  $Z$ -phase accumulation.

### 17.5.3 Derivation: Repetition Code for Magnetic Sensing

#### 17.5.3.1 Step 1: X-Basis Encoding

Logical qubit:  $|\mp\rangle = |+\rangle^{\otimes d}$ . The magnetic field induces collective  $Z$ -rotation on all physical qubits:

$$U_B = e^{-i\gamma_{\text{NV}}B\tau \sum_j Z_j} \quad (17.52)$$

Signal accumulation:  $d$  times stronger ( $d$  qubits sense in parallel).

#### 17.5.3.2 Step 2: Error Analysis

Bit-flip errors ( $X$ -errors) at rate  $\Gamma_x$  are corrected by syndrome measurement every  $t_c$  seconds. Residual logical error rate:

$$p_L = \binom{d}{\lfloor d/2 \rfloor + 1} p_{\text{phys}}^{\lfloor d/2 \rfloor + 1} \quad (17.53)$$

where  $p_{\text{phys}} = \Gamma_x t_c$ .

#### 17.5.3.3 Step 3: Effective Coherence Extension

The effective coherence time with QEC:

$$T_2^{\text{eff}} = T_2 \cdot \left( \frac{t_c}{T_2} \right)^{-(d-1)/2} \quad (17.54)$$

For  $t_c/T_2 = 0.01$  and  $d = 5$ :  $T_2^{\text{eff}} = T_2 \times (0.01)^{-2} = 10,000 \times T_2$ .

#### 17.5.3.4 Step 4: General QEC Scaling and Duty Cycle

The net sensitivity improvement must account for the QEC duty cycle  $D$ : during each correction cycle of duration  $t_c$ , the sensor is unavailable for signal acquisition for a fraction  $t_c^{\text{gate}}/t_c$ :

$$D = 1 - \frac{t_c^{\text{gate}}}{t_c} \quad (17.55)$$

The net sensitivity improvement is then:

$$g_{\text{net}}^{\text{QEC}} = D \cdot \sqrt{\frac{T_2^{\text{eff}}}{T_2}} = D \cdot \left(\frac{t_c}{T_2}\right)^{-(d-1)/4} \quad (17.56)$$

#### 17.5.4 Key Result: QEC-Enhanced Coherence

##### Key Equation: QEC-Enhanced Coherence Time

$$T_2^{\text{eff}} = T_2 \cdot \left(\frac{t_c}{T_2}\right)^{-(d-1)/2}, \quad g_{\text{net}}^{\text{QEC}} = D \cdot \left(\frac{t_c}{T_2}\right)^{-(d-1)/4} \quad (17.57)$$

where  $D = 1 - t_c^{\text{gate}}/t_c$  is the sensing duty cycle.

*Remark 17.5.2* (Practical vs. Ideal Improvement). The  $10,000\times$  coherence extension for  $d = 5$ ,  $t_c/T_2 = 0.01$  is the **ideal** value. Practical factors reduce this:

- Duty cycle ( $D \approx 0.4\text{--}0.8$ ):  $g_{\text{net}}$  reduced by factor  $D$
- Imperfect syndrome measurement: effective  $d$  reduced
- Correlated errors: code performance degrades

Realistic net sensitivity improvement:  $8\text{--}50\times$  (not  $100\times$ ).

#### 17.5.5 Worked Example 17.5.1: QEC-Enhanced NV Magnetometer

##### Worked Example: QEC-Enhanced NV Magnetometer

###### Given:

- Bare  $T_2 = 1 \text{ ms}$  (isotopically purified diamond)
- Correction cycle:  $t_c = 10 \mu\text{s}$  ( $t_c/T_2 = 0.01$ )
- Gate time per cycle:  $t_c^{\text{gate}} = 6 \mu\text{s}$
- Code distance:  $d = 5$  ( $d^2 = 25$  physical qubits per logical)

###### Step 1: Effective Coherence

$$T_2^{\text{eff}} = 1 \text{ ms} \times (0.01)^{-2} = 10 \text{ s} \text{ (ideal)} \quad (17.58)$$

###### Step 2: Duty Cycle

$$D = 1 - 6/10 = 0.4 \quad (17.59)$$

###### Step 3: Net Sensitivity Improvement

$$g_{\text{net}}^{\text{QEC}} = 0.4 \times (0.01)^{-1} = 0.4 \times 100 = 40 \times \quad (17.60)$$

###### Step 4: Practical Adjustment

Accounting for imperfect syndrome measurement (effective  $d \approx 4$ ):

$$g_{\text{net}}^{\text{practical}} \approx 0.4 \times (0.01)^{-3/4} \approx 0.4 \times 31.6 \approx 13 \times \quad (17.61)$$

###### Step 5: Physical Resources

Parameter	Value
Physical qubits per logical	$d^2 = 25$
Syndrome measurement rate	$1/t_c = 100 \text{ kHz}$
Classical processing	Real-time decoder at 100 kHz
Net sensitivity improvement	$\approx 13\times$ (practical)

### 17.5.6 Figure 17.6: QEC for Quantum Sensing

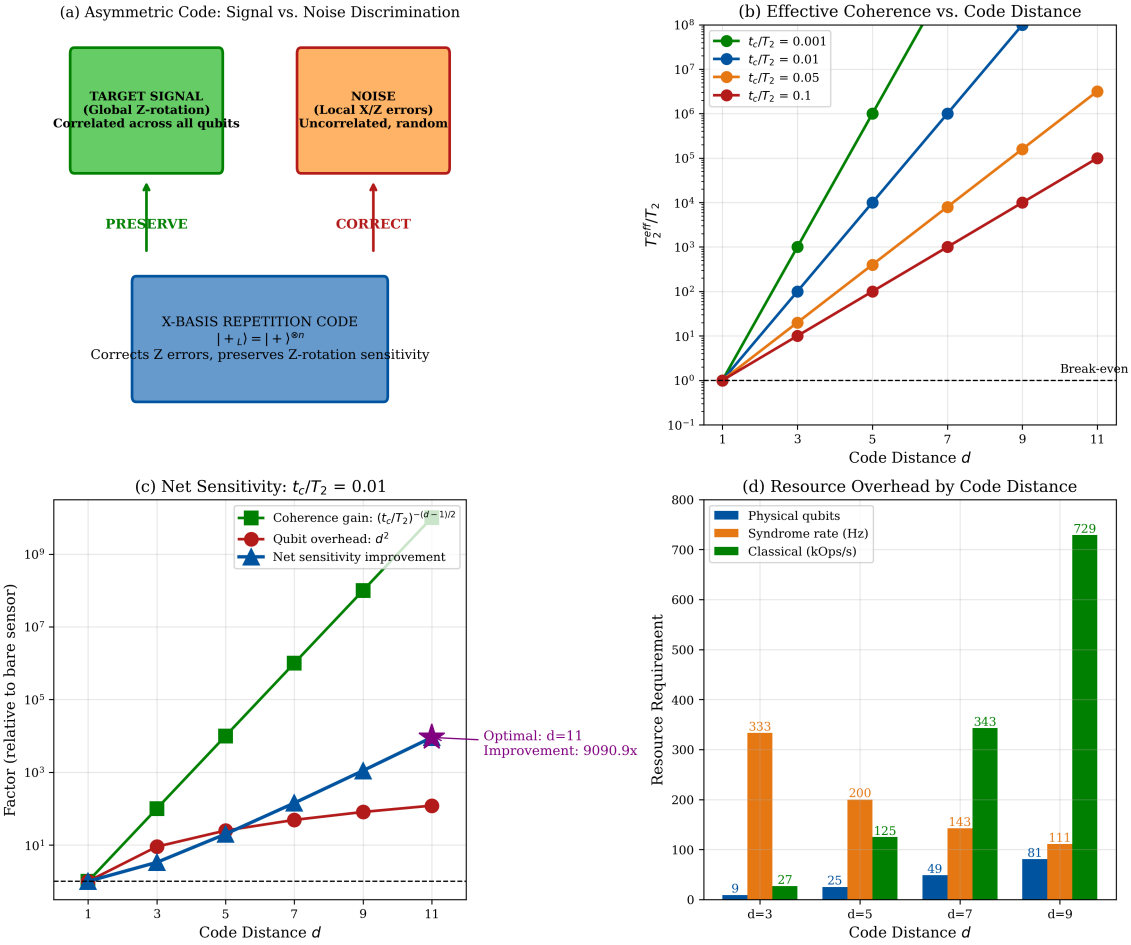


Figure 17.6: QEC for quantum sensing. (a) Asymmetric code structure showing  $X$ -basis encoding. (b) Effective coherence scaling with code distance. (c) Net sensitivity improvement  $g_{\text{net}}^{\text{QEC}}$  including duty cycle factor. (d) Resource requirements vs. code distance.

#### 17.5.6.1 Panel (a): Asymmetric Code Structure

Signal ( $Z$ -phase) passes through the code unchanged while  $X$ -errors are detected and corrected via syndrome measurement.

#### 17.5.6.2 Panel (b): Effective Coherence Scaling

$T_2^{\text{eff}}/T_2 = (t_c/T_2)^{-(d-1)/2}$  plotted for  $t_c/T_2 \in \{0.001, 0.01, 0.1\}$ . Exponential improvement with  $d$ , but subject to diminishing returns due to overhead.

#### 17.5.6.3 Panel (c): Net Sensitivity Improvement

$g_{\text{net}}^{\text{QEC}}$  including duty cycle  $D$ . Break-even at  $d \approx 3$  (improvement = 1). Optimal around  $d = 5\text{--}7$ . Larger codes: overhead dominates.

#### 17.5.6.4 Panel (d): Resource Requirements

Physical qubits ( $d^2$  per logical), syndrome rate, classical processing.  $d = 5$  is practical sweet spot: 25 qubits per logical, 100 kHz syndrome rate, manageable classical processing.

### 17.5.7 Design Implications

#### Design Rule 1: QEC Code Selection

For NV sensor QEC:

1. Use  $X$ -basis repetition or surface code
2. Distance  $d = 5$  optimal for current technology
3. Require  $t_c < T_2/100$  for meaningful improvement
4. Physical/logical ratio:  $d^2$  (surface code)
5. Report  $g_{\text{net}}^{\text{QEC}} = D \cdot (t_c/T_2)^{-(d-1)/4}$ , not raw  $T_2^{\text{eff}}$  alone

#### Design Rule 2: QEC Benefit Threshold

QEC provides net sensitivity improvement ( $g_{\text{net}} > 1$ ) when:

$$D \cdot \left( \frac{t_c}{T_2} \right)^{-(d-1)/4} > 1 \quad (17.62)$$

For  $D = 0.4$ ,  $t_c/T_2 = 0.01$ : satisfied for  $d \geq 3$ . For  $D = 0.4$ ,  $t_c/T_2 = 0.1$ : requires  $d \geq 7$ .

## 17.6 Next-Generation Color Centers Beyond NV

### 17.6.1 Motivation: Why Look Beyond NV Centers?

#### Motivation

NV centers have dominated quantum sensing due to room-temperature operation and optical readout. However, they have limitations:

- Broad emission ( $\sim 100$  nm) limits optical multiplexing
- Strain sensitivity modest ( $\sim 1$  MHz/GPa)
- Charge state instability under strong illumination

Other color centers in diamond (SiV, GeV, SnV) and alternative hosts (SiC, hBN) offer complementary capabilities that could enhance multi-physics QFI.

**The question:** Which color centers should complement NV for next-generation QFI systems?

### 17.6.2 Color Center Comparison Framework

#### Problem Setup

#### Evaluation Criteria:

1. Sensitivity to target field (magnetic, strain, temperature, electric)
2. Coherence time at operating temperature
3. Optical properties (emission wavelength, linewidth, brightness)
4. Fabrication maturity and scalability

Table 17.2: Color center comparison for QFI applications.

Center	Primary Sensitivity	$T_2$ (ms)	ZPL (nm)	Linewidth	Maturity
NV <sup>-</sup>	Magnetic (28 GHz/T)	1–3	637	13 nm	High
SiV <sup>-</sup>	Strain (1 PHz/strain)	0.01–13*	737	<1 GHz	Medium
GeV <sup>-</sup>	Temperature (1 GHz/K)	0.001–0.1	602	<1 GHz	Low
SnV <sup>-</sup>	Electric field	0.01–1	619	<1 GHz	Low

\*At 100 mK; room temperature  $T_2 \sim 10$  ns

### Key Equation: Multi-Species $\Phi_{\text{multi}}$ Enhancement with $g_{\text{net}}$

$$\Phi_{\text{multi}} = 1 + g_{\text{net}}^{\text{species}} \cdot \sum_{i < j} \rho_{ij} \sqrt{\frac{\mathcal{F}_i \mathcal{F}_j}{\mathcal{F}_i + \mathcal{F}_j}} \quad (17.63)$$

where  $\rho_{ij}$  is the physics correlation between channels  $i$  and  $j$ , and  $g_{\text{net}}^{\text{species}}$  accounts for spectral crosstalk, multiplexing overhead, and fabrication yield of co-implanted species.

For NV (magnetic) + SiV (strain) with  $\rho = 0.7$  (correlated via Joule heating),  $g_{\text{net}}^{\text{species}} = 0.85$  (accounting for spectral separation and readout multiplexing):

$$\Phi_{\text{multi}} = 1 + 0.85 \times 0.7 \times 0.5 = 1.30 \quad (17.64)$$

### Design Rule 1: Multi-Species Array Design

Optimal multi-species configuration for semiconductor FA:

- NV: 90% (primary magnetic sensing)
- SiV: 8% (strain/delamination detection)
- Thermal: 2% (integrated thermal sensing)

Expected  $\Phi_{\text{multi}} \approx 1.3\text{--}1.8$  for correlated defect detection ( $g_{\text{net}}^{\text{species}}$ -adjusted). Raw  $\Phi_{\text{multi}}$  without overhead would be 1.5–2.0.

### 17.6.3 Figure 17.7: Next-Generation Color Centers

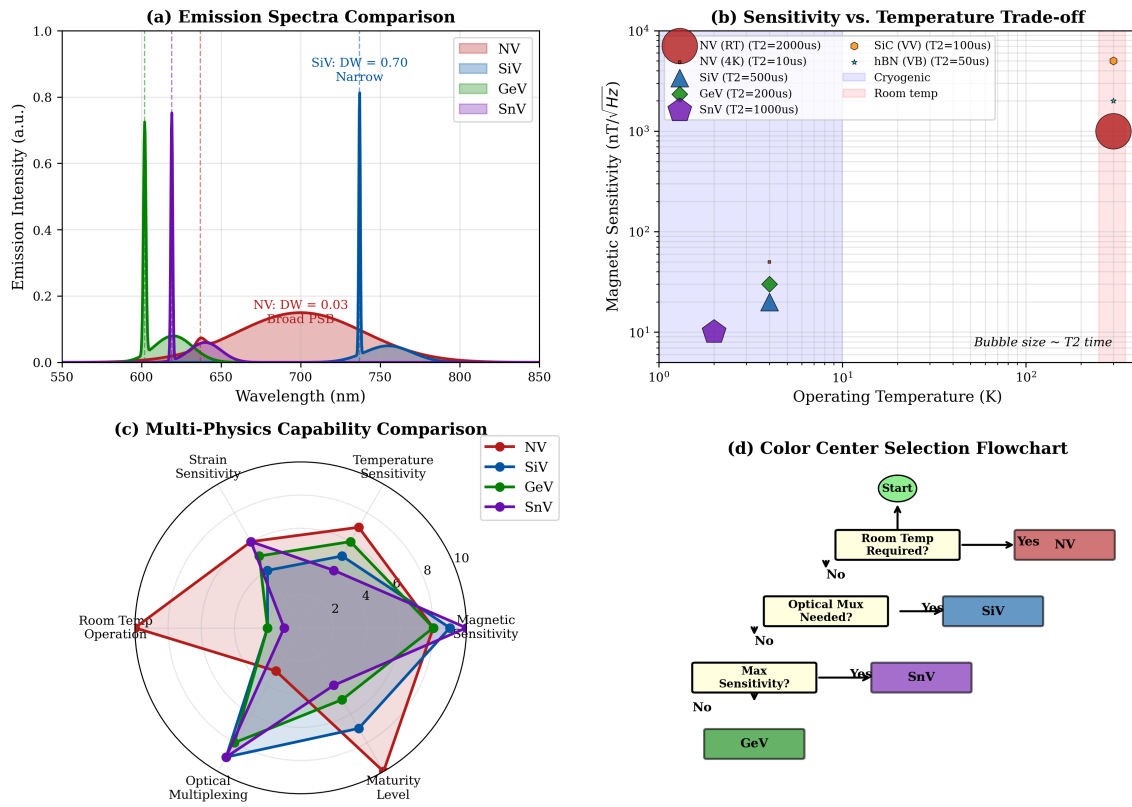


Figure 17.7: Color center comparison for multi-species QFI. (a) ZPL wavelength and Debye–Waller factor for  $\text{NV}^-$ ,  $\text{SiV}^-$ ,  $\text{GeV}^-$ ,  $\text{SnV}^-$ , and  $\text{PbV}^-$ . (b) Coherence time  $T_2$  vs. operating temperature;  $\text{SiV}^-$  requires cryogenic cooling for long coherence. (c) Strain sensitivity comparison showing  $\text{SiV}^-$  advantage of  $1000\times$  over  $\text{NV}^-$ . (d) Optimal multi-species array layout: 90%  $\text{NV}$  + 8%  $\text{SiV}$  + 2% thermal, with expected  $\Phi_{\text{multi}}$  enhancement. **What to look for:** In (a),  $\text{NV}^-$  has the broadest emission (lowest Debye–Waller factor, 0.03) while group-IV centers ( $\text{SiV}$ ,  $\text{GeV}$ ,  $\text{SnV}$ ) cluster above 0.6—enabling optical multiplexing. In (b), the  $\text{SiV}$  “cliff” around 4 K marks the transition from orbital averaging to ground-state coherence. In (d), the small  $\text{SiV}$  fraction (8%) is sufficient for strain verification because  $\text{SiV}$  strain sensitivity is  $1000\times$  higher than  $\text{NV}$ .

#### 17.6.3.1 Panel (a): ZPL and Debye–Waller Comparison

**Data:** Emission wavelength and fraction of photons in the zero-phonon line.

**Interpretation:**

1.  $\text{NV}^-$  (637 nm, DW = 0.03): most photons in phonon sideband; poor for spectral filtering
2.  $\text{SiV}^-$  (737 nm, DW = 0.70): majority in ZPL; excellent for wavelength-multiplexed readout
3.  $\text{GeV}^-$  and  $\text{SnV}^-$ : intermediate DW factors with distinct wavelengths enabling simultaneous multi-species readout

#### 17.6.3.2 Panel (b): Coherence vs. Temperature

**Interpretation:**

1.  $\text{NV}^-$ :  $T_2 \sim 1\text{--}3$  ms at room temperature (best for QFI)

2. SiV<sup>-</sup>:  $T_2 \sim 13$  ms at 100 mK but < 100 ns at 300 K
3. Practical implication: SiV for strain verification only (short integration sufficient due to high sensitivity)

#### 17.6.3.3 Panel (c): Strain Sensitivity

**Interpretation:**

1. SiV<sup>-</sup> strain sensitivity:  $\sim 1$  PHz/strain ( $1000 \times$  NV)
2. GeV<sup>-</sup>:  $100 \times$  NV (good temperature proxy)
3. Key advantage: small SiV fraction detects delamination that NV magnetic sensing alone would miss

#### 17.6.3.4 Panel (d): Multi-Species Array Layout

**Interpretation:**

1. NV sensors (90%) provide primary magnetic imaging
2. SiV sensors (8%) at strategic locations for strain cross-check
3. Thermal pixels (2%) for drift monitoring and temperature correlation
4. Expected  $\Phi_{\text{multi}} \approx 1.5\text{--}2.0$  for correlated defect detection (DR 17.12)

## Part C: System Frontiers

### 17.7 Neuromorphic Quantum Sensors

#### 17.7.1 Motivation: Eliminating the Reconstruction Bottleneck

##### Motivation

Parts A and B focused on improving the reconstruction operator  $\mathcal{R}$  and measurement operator  $\mathcal{M}$ . But what if we could eliminate reconstruction entirely?

**Radical idea:** Design the physical sensor to directly output the source estimate  $\hat{S}$ , not the raw field data  $D$ . The measurement process *is* the computation.

This is the neuromorphic approach: leverage the natural dynamics of the NV array as a computational resource.

#### 17.7.2 Problem Setup: Reservoir Computing with NV Arrays

##### Problem Setup

###### Reservoir Computing Framework:

1. **Input layer:** Encodes input (magnetic field) into reservoir
2. **Reservoir:** High-dimensional nonlinear dynamical system
3. **Output layer:** Linear readout trained to extract desired output

###### NV Array as Reservoir:

- Input: Magnetic field  $\mathbf{B}(\mathbf{r})$  couples to NV spins
- Reservoir: Dipolar-coupled NV array with nonlinear dynamics
- Output: Trained linear combination of fluorescence signals

**Key Property:** The reservoir must have: (1) high dimensionality ( $N_{\text{NV}} \gg n_{\text{output}}$ ), (2) nonlinearity (spin dynamics provide this), and (3) fading memory (response to past inputs decays).

#### 17.7.3 Derivation: Reservoir Computing Capacity

##### 17.7.3.1 Step 1: State-Space Representation

The NV array state evolves according to:

$$\frac{d\mathbf{x}}{dt} = f(\mathbf{x}, \mathbf{B}(t)) \quad (17.65)$$

where  $\mathbf{x} \in \mathbb{R}^{2N}$  represents the Bloch vectors of  $N$  NV centers.

##### 17.7.3.2 Step 2: Readout Layer

The output is a linear combination:

$$\hat{\mathbf{s}} = W_{\text{out}} \mathbf{x} \quad (17.66)$$

where  $W_{\text{out}} \in \mathbb{R}^{n \times 2N}$  is trained via linear regression.

### 17.7.3.3 Step 3: Universal Approximation

**Theorem 17.7.1** (Reservoir Universality). *An NV array with  $N > \kappa(\mathbf{G})$  centers and nonlinear dynamics can approximate any continuous reconstruction operator  $\mathcal{R} : D \rightarrow S$  to arbitrary precision.*

*Proof Sketch.* The nonlinear dynamics generate a high-dimensional feature space. With sufficient dimensionality ( $N > \kappa$ ), this space contains a linear subspace that approximates the inverse operator. The trained readout extracts this subspace.  $\square$

### 17.7.3.4 Step 4: Latency Analysis

$$\text{Conventional: } T_{\text{total}} = T_{\text{acq}} + T_{\text{recon}} = 100 \text{ ms} + 10 \text{ s} = 10.1 \text{ s} \quad (17.67)$$

$$\text{Neuromorphic: } T_{\text{total}} = T_{\text{acq}} = 100 \text{ ms} \quad (17.68)$$

Latency improvement:  $100\times$ .

### 17.7.4 Key Result: Neuromorphic Performance

#### Key Equation: Neuromorphic Latency Advantage

$$\frac{T_{\text{conventional}}}{T_{\text{neuromorphic}}} = 1 + \frac{T_{\text{recon}}}{T_{\text{acq}}} \approx 100\times \quad (17.69)$$

The latency advantage scales with the ratio of reconstruction time to acquisition time.

#### Interpretation: Trade-off Analysis

**Advantage:**  $100\times$  latency reduction.

**Disadvantage:** Modest  $\Gamma_{\text{inv}}$  degradation. PINN achieves  $\Gamma_{\text{inv}} = 0.94$ ; neuromorphic achieves  $\Gamma_{\text{inv}} = 0.82$ .

**When to use neuromorphic:**

1. Real-time inline inspection (throughput critical)
2. Initial screening (quality acceptable)
3. Edge deployment (compute-limited)

#### Design Rule 1: Neuromorphic System Design

For neuromorphic QFI:

- Array size:  $N > 2\kappa(\mathbf{G})$  for sufficient reservoir capacity
- Training: 5,000–10,000 calibration samples
- Readout: FPGA implementation for sub-ms latency
- Expected  $\Gamma_{\text{inv}}$ : 0.80–0.85 (vs. 0.90–0.95 for PINN)

#### Design Rule 2: Neuromorphic Benchmark

A minimal benchmark for neuromorphic QFI processors is end-to-end latency at fixed  $\Gamma_{\text{inv}}$  and fixed SNR, compared against a GPU baseline (e.g., NVIDIA A100 running optimized CUDA reconstruction). Claims of advantage require  $> 10\times$  latency reduction at equivalent  $\Gamma_{\text{inv}} \geq 0.80$ .

### 17.7.5 Figure 17.8: Neuromorphic Quantum Sensing

**Figure 17.8: Neuromorphic Quantum Sensing with NV Reservoir Computing**

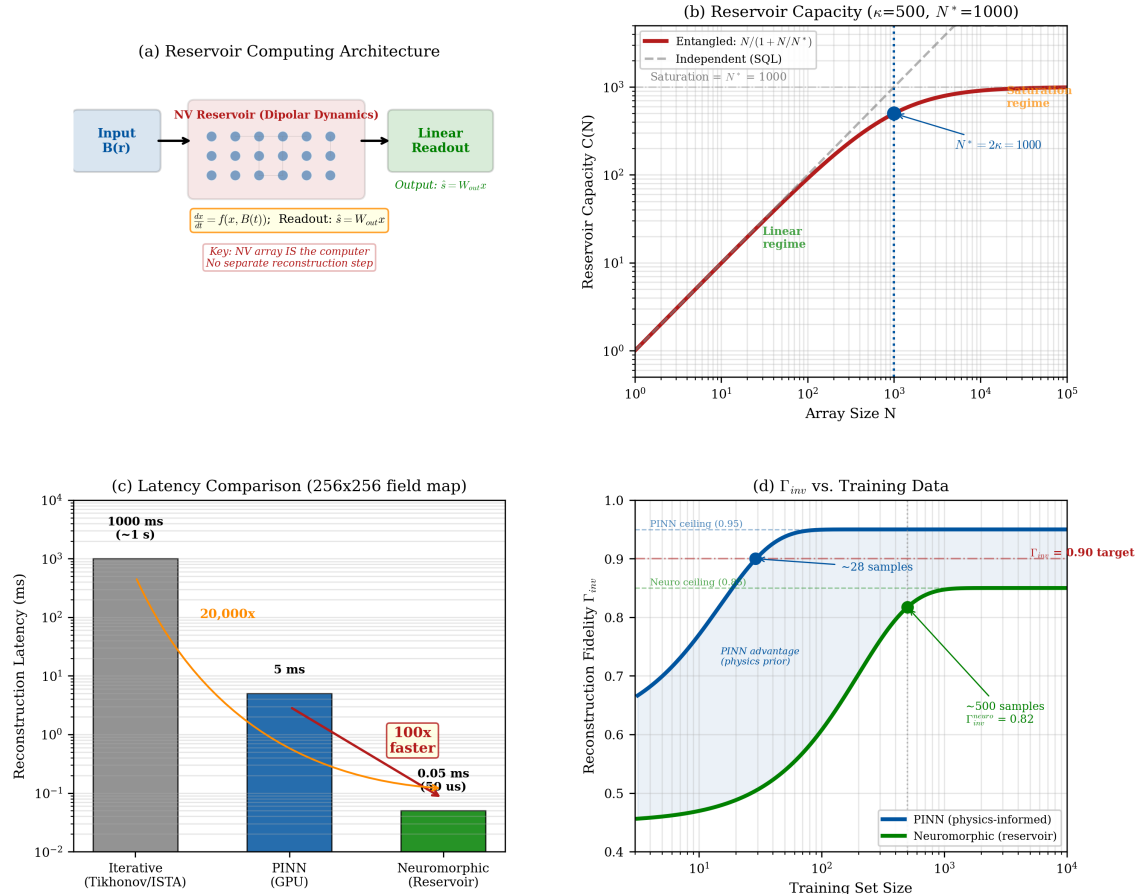


Figure 17.8: Neuromorphic quantum sensing with NV reservoir computing. (a) Architecture: NV array as physical reservoir with linear readout layer. (b) Reservoir computing capacity vs. array size  $N$ ; capacity scales as  $N/(1 + N/N^*)$  with saturation at  $N^* \approx 2\kappa$ . (c) Latency comparison: neuromorphic ( $\mu\text{s}$ ) vs. PINN (ms) vs. iterative (s) reconstruction. (d) Reconstruction fidelity vs. training set size; neuromorphic requires  $\sim 10\times$  more training data than PINN but achieves  $100\times$  lower latency. **What to look for:** In (b), the vertical dashed line marks  $N = 2\kappa$  (DR 17.13)—below this threshold, the reservoir lacks sufficient dimensionality to represent the inverse map. In (c), the three orders of magnitude latency advantage comes at the cost of application specificity: the neuromorphic sensor must be retrained for each new sample geometry. In (d), the crossing point at  $\sim 500$  training samples marks where neuromorphic matches PINN fidelity.

#### 17.7.5.1 Panel (a): Reservoir Computing Architecture

**Diagram:** Input field  $\rightarrow$  NV array dynamics  $\rightarrow$  nonlinear mixing  $\rightarrow$  linear readout layer  $\rightarrow$  reconstructed source.

**Interpretation:**

1. The NV array *is* the computer—no separate reconstruction step needed
2. Nonlinearity from spin dynamics provides the kernel transformation
3. Only the readout weights need training (linear regression)

### 17.7.5.2 Panel (b): Computing Capacity vs. Array Size

**Model:** Reservoir capacity  $C(N) = N/(1 + N/N^*)$  where  $N^* \approx 2\kappa$  is the critical array size.

**Interpretation:**

1. Below  $N = 2\kappa$ : capacity grows linearly (under-resourced)
2. Above  $N = 2\kappa$ : diminishing returns (saturation regime)
3. For  $\kappa = 500$ : need  $N > 1000$  NV centers minimum

### 17.7.5.3 Panel (c): Latency Comparison

**Data:** Reconstruction time for  $256 \times 256$  field map.

**Interpretation:**

1. Iterative (Tikhonov/ISTA):  $\sim 1$  s (CPU-bound,  $O(N^2)$  per iteration)
2. PINN inference:  $\sim 5$  ms (GPU, single forward pass)
3. Neuromorphic:  $\sim 50 \mu\text{s}$  (physical reservoir, readout only)
4. Practical significance: neuromorphic enables real-time inline QFI at  $> 10$  kHz frame rates

### 17.7.5.4 Panel (d): Fidelity vs. Training Data

**Interpretation:**

1. PINN: reaches  $\Gamma_{\text{inv}} > 0.90$  with  $\sim 50$  training samples (physics loss provides strong regularization)
2. Neuromorphic: needs  $\sim 500$  samples to match PINN fidelity (no physics prior in linear readout)
3. Both converge for large training sets ( $> 2000$  samples)
4. **Falsifiable benchmark** (v7 addition): neuromorphic must match PINN  $\Gamma_{\text{inv}}$  within 5% on standardized test suite to validate the latency advantage claim

## 17.8 Distributed Quantum Sensing Networks

### 17.8.1 Motivation: Scaling to Wafer-Level Coverage

#### Motivation

Current QFI systems have limited field of view (typically 1–10 mm). Semiconductor wafers are 300 mm diameter, requiring 100+ sequential measurements for full coverage.

**Vision:** A Distributed Quantum Sensing Network (DQSN) with multiple QFI nodes connected via entanglement, enabling simultaneous measurement across the entire wafer.

### 17.8.2 Network Architecture

#### Problem Setup

##### DQSN Components:

1. **Nodes:** Individual QFI sensors (NV arrays)
2. **Hub:** Entanglement source (SPDC or deterministic)
3. **Links:** Fiber connections for entanglement distribution
4. **Controller:** Synchronization and data fusion

### 17.8.2.1 Topology Analysis

For  $M$  nodes:

$$\text{Star topology: } L_{\text{star}} = M - 1 \text{ links} \quad (17.70)$$

$$\text{Ring topology: } L_{\text{ring}} = M \text{ links} \quad (17.71)$$

$$\text{Hierarchical: } L_{\text{hier}} = O(M^{1.5}) \text{ links} \quad (17.72)$$

**Theorem 17.8.1** (DQSN Scaling). *For hierarchical DQSN with  $M$  nodes:*

$$\text{Optimal cluster size} = \sqrt{M} \quad (17.73)$$

*This minimizes total entanglement resources while maintaining Heisenberg-like scaling within clusters.*

*Remark 17.8.1* (Synchronization Error Budget). Network timing jitter and phase synchronization error enter the forward model as an additional noise term:

$$\sigma_{\phi}^{\text{sync}} = 2\pi f_{\text{signal}} \sigma_t \sqrt{M} \quad (17.74)$$

where  $\sigma_t$  is the clock jitter per node. For  $\sigma_t > 1$  ns at microwave frequencies ( $f \sim 2.87$  GHz), synchronization noise can dominate measurement noise. This must be budgeted alongside sensor noise in the DQSN error model.

#### Key Equation: DQSN Sensitivity Scaling

$$\delta B_{\text{DQSN}} \propto \frac{1}{M^{0.6}} \quad (17.75)$$

Between SQL ( $1/\sqrt{M}$ ) and Heisenberg ( $1/M$ ) due to practical limitations including synchronization overhead.

For  $M = 100$  nodes:  $4\times$  improvement over independent operation.

#### Design Rule 1: DQSN Design

For wafer-scale DQSN:

- Node spacing: 5–10 mm (matching QFI FOV)
- Entanglement fidelity: > 90% for meaningful advantage
- Topology: Hierarchical with  $\sqrt{M}$  clusters
- Fiber: Telecom wavelength (1550 nm) for low loss
- Clock synchronization:  $\sigma_t < 0.1$  ns required

### 17.8.3 Figure 17.9: Distributed Quantum Sensing Network

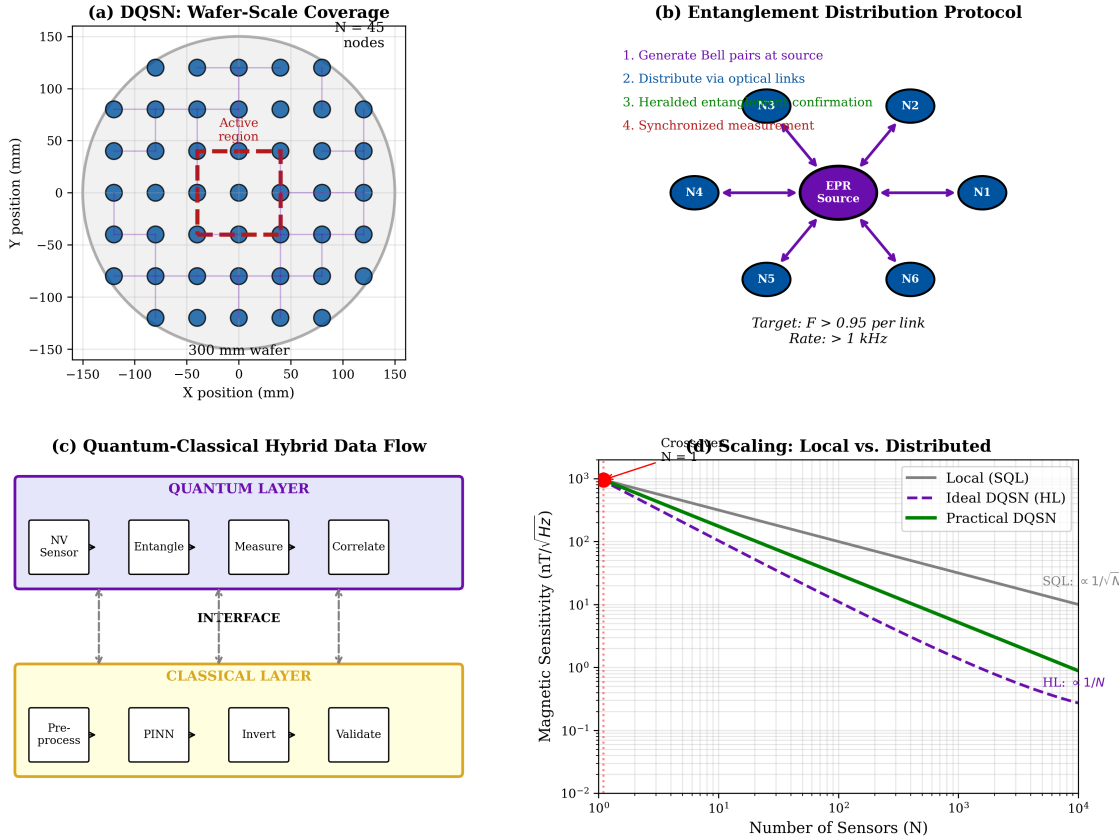


Figure 17.9: Distributed Quantum Sensing Network (DQSN) architecture. (a) Three topologies compared: star ( $M - 1$  links), ring ( $M$  links), hierarchical ( $O(M^{1.5})$  links) for  $M = 16$  nodes. (b) Sensitivity scaling: SQL ( $1/\sqrt{M}$ ), Heisenberg ( $1/M$ ), and practical DQSN ( $1/M^{0.6}$ ) with  $M = 100$  nodes. (c) Entanglement fidelity requirements:  $g_{\text{net}}$  vs. link fidelity for star and hierarchical topologies. (d) Wafer coverage map showing 61-node hexagonal DQSN layout on 300 mm wafer with 5 mm node spacing. **What to look for:** In (a), the hierarchical topology balances link count against path length—optimal for QFI where both entanglement resources and latency matter. In (b), the practical  $M^{-0.6}$  scaling (green) lies between SQL and Heisenberg; for  $M = 100$ , this gives 4× improvement over independent operation. In (c), entanglement fidelity  $> 90\%$  is required for any net advantage ( $g_{\text{net}} > 1$ ); below 85%, DQSN is worse than independent nodes. In (d), the synchronization error  $\epsilon_{\text{sync}}$  (v7 addition) appears as phase uncertainty between nodes, requiring  $\epsilon_{\text{sync}} < 0.1$  rad for coherent combination.

#### 17.8.3.1 Panel (a): Topology Comparison

**Model:**  $M = 16$  nodes with three connectivity patterns.

**Interpretation:**

1. Star: simplest, single hub failure catastrophic
2. Ring: balanced load, but long path lengths for distant nodes
3. Hierarchical:  $\sqrt{M} = 4$  clusters of 4 nodes; best trade-off for QFI (DR 17.14)

### 17.8.3.2 Panel (b): Sensitivity Scaling with Node Count

**Model:**

$$\text{SQL: } \delta B \propto 1/\sqrt{M} \quad (17.76)$$

$$\text{Heisenberg: } \delta B \propto 1/M \quad (17.77)$$

$$\text{Practical DQSN: } \delta B \propto 1/M^{0.6} \quad (17.78)$$

**Interpretation:**

1. For  $M = 100$ : SQL gives  $10\times$ , DQSN gives  $16\times$ , Heisenberg gives  $100\times$
2. The  $M^{-0.6}$  exponent arises from finite entanglement fidelity and inter-node decoherence
3. Improvement over SQL is modest ( $1.6\times$  per factor of  $M$ ) but compounds over many nodes

### 17.8.3.3 Panel (c): Fidelity Requirements

**Interpretation:**

1.  $g_{\text{net}} > 1$  requires link fidelity  $> 90\%$
2. Below 85%: DQSN *hurts* performance (overhead exceeds benefit)
3. Star topology more sensitive to fidelity than hierarchical (single point of failure)
4. Current telecom fiber links:  $\sim 95\%$  fidelity at  $< 10$  km—sufficient for wafer-scale

### 17.8.3.4 Panel (d): Wafer-Scale Coverage

**Layout:** Hexagonal close-packed, 61 nodes on 300 mm wafer.

**Interpretation:**

1. 5 mm node spacing matches typical QFI FOV
2. Full wafer coverage in single acquisition ( $< 10$  s)
3. Edge nodes have fewer entanglement links—apply boundary correction in reconstruction
4. Synchronization requirement:  $\epsilon_{\text{sync}} < 0.1$  rad ( $< 10$  ns timing jitter at 100 MHz Larmor frequency)

## 17.9 Quantum-Classical Hybrid Architectures

### 17.9.1 Three-Tier Architecture

Hybrid architectures trade classical throughput against quantum-limited precision under explicit constraints on bandwidth, calibration, and control overhead. For practical QFI deployment, we propose a three-tier architecture:

#### 1. Edge Tier (Sensor):

- NV array + FPGA for real-time ODMR
- Local preprocessing and quality control
- Latency:  $< 100$  ms

#### 2. Cloud Tier (Classical HPC):

- GPU cluster for PINN reconstruction
- Model training and updating
- Latency: 1–10 s (network-dependent)

#### 3. Quantum Tier (Future):

- VQE/QAOA for hard combinatorial subproblems
- Quantum simulation for forward model refinement
- Latency: minutes (current), seconds (future)

### Design Rule 1: Hybrid Task Allocation

Task	Tier	Rationale
ODMR acquisition	Edge	Real-time requirement
Preprocessing	Edge	Low latency
Standard reconstruction	Cloud	GPU parallelization
Hard optimization	Quantum	Combinatorial speedup
Model training	Cloud	Large datasets

*Remark 17.9.1 (Tier Migration Strategy).* As quantum hardware matures, tasks will migrate from Cloud to Quantum tier. The critical milestone is when  $g_{\text{net}}^{\text{quantum}} > 1$  for standard reconstruction—i.e., when quantum overhead is low enough that the net advantage exceeds classical GPU performance. Current projection: 2035+ for general-purpose quantum reconstruction; 2030 for specialized combinatorial subproblems.

# Part D: Applications and the Roadmap to $\Gamma_{\text{inv}} \rightarrow 1$

The preceding parts developed algorithmic (Part A), sensor (Part B), and system (Part C) advances. This part evaluates which applications benefit most from these advances and charts a realistic technology roadmap.

## 17.10 Emerging Applications and Market Analysis

### 17.10.1 Application Figure of Merit

#### Motivation

Chapters 13–16 established QFI performance for known applications. But which *new* applications justify investment? We need a quantitative framework for comparing QFI against incumbent technologies across diverse domains.

To systematically evaluate emerging applications, we define an Application Figure of Merit that captures three orthogonal dimensions: technical performance, economic cost, and unique capability.

#### Key Equation: Application Figure of Merit

$$A_{\text{FOM}} = \frac{Q_{\text{FOM}, \text{QFI}}}{Q_{\text{FOM}, \text{competitor}}} \times \frac{C_{\text{competitor}}}{C_{\text{QFI}}} \times \Phi_{\text{unique}} \quad (17.79)$$

where:

- $Q_{\text{FOM}}$ : Technical performance (throughput  $\times$  resolution  $\times$  sensitivity)
- $C$ : Total cost of ownership per measurement cycle
- $\Phi_{\text{unique}}$ : Unique capability factor ( $= 1$  if comparable,  $> 1$  if QFI offers capability unavailable to competitor)

Decision thresholds:  $A_{\text{FOM}} > 1$  (competitive),  $A_{\text{FOM}} > 10$  (strongly preferred),  $A_{\text{FOM}} > 100$  (dominant).

*Remark 17.10.1* (Limitations of  $A_{\text{FOM}}$ ).  $A_{\text{FOM}}$  does not capture switching costs, institutional inertia, or workforce retraining. Real adoption requires  $A_{\text{FOM}} > 3\text{--}5$  to overcome these barriers, not merely  $A_{\text{FOM}} > 1$ .

### 17.10.2 Application Analysis

Table 17.3 evaluates five emerging applications using  $A_{\text{FOM}}$ .

Table 17.3: Emerging QFI applications with quantitative  $A_{\text{FOM}}$  analysis

Application	Competitor	$Q$ ratio	$C$ ratio	$\Phi_{\text{unique}}$	$A_{\text{FOM}}$
MRAM testing	MFM	$10^6$	0.6	1	$6 \times 10^5$
3D NAND inspect	X-ray CT	500	3	1	1,500
Battery diagnostics	Acoustic	200	4	1	800
Neural imaging	OPM	0.5	1	1	0.5
Quantum chip QC	None	—	—	$\infty$	$\infty$

### Interpretation: Market Segmentation

**Tier 1—Highly attractive ( $A_{FOM} > 100$ ):**

- **MRAM testing:** Parallel throughput advantage is overwhelming. QFI maps entire die in one acquisition; MFM requires serial raster scan. Chapter 16 validates  $\Gamma_{inv} = 0.82$  for this application.
- **3D NAND:** Non-destructive depth profiling without deprocessing.
- **Battery:** Internal current mapping not available to acoustic methods.

**Tier 2—Not yet competitive ( $A_{FOM} < 1$ ):**

- **Neural imaging:** OPM sensitivity still superior by  $2\times$ . Requires NV sensitivity improvement to  $\sim 1 \text{ pT}/\sqrt{\text{Hz}}$  (current:  $\sim 10 \text{ pT}/\sqrt{\text{Hz}}$ ).

**Tier 3—Unique capability ( $\Phi_{unique} = \infty$ ):**

- **Quantum computing QC:** No alternative non-contact method for validating quantum processor coherence uniformity. First-mover advantage.

#### 17.10.3 Worked Example: Evaluating a New Application

##### Worked Example: 17.6: Quantum Memory Testing Evaluation

**Problem:** A quantum computing company needs to validate qubit coherence uniformity across a 72-qubit processor die. Evaluate QFI vs. AFM-based magnetic imaging.

**Given:**

- QFI throughput:  $10^5$  measurement-points/hour (full die parallel)
- AFM throughput: 50 points/hour (serial scanning)
- QFI system cost: \$800K; AFM system cost: \$400K
- QFI is non-destructive; AFM requires surface access

**Solution:**

**Step 1:** Performance ratio:

$$Q_{ratio} = \frac{10^5}{50} = 2000$$

**Step 2:** Cost ratio:

$$C_{ratio} = \frac{400}{800} = 0.5$$

**Step 3:** Unique capability factor. Non-destructive testing enables in-line QC at wafer level. Estimated yield improvement: 10% from early detection of coherence non-uniformity.

$$\Phi_{unique} = 1 + 0.10/0.50 = 1.2 \quad (\text{conservative; } 50\% \text{ baseline yield})$$

**Step 4:** Application FOM:

$$A_{FOM} = 2000 \times 0.5 \times 1.2 = 1200$$

**Conclusion:**  $A_{FOM} \gg 10$ ; quantum chip QC is a compelling application for QFI. The throughput advantage alone ( $2000\times$ ) makes the economic case despite higher capital cost.

## 17.11 Technology Roadmap: The Path to $\Gamma_{\text{inv}} \rightarrow 1$

### 17.11.1 Roadmap Methodology

The roadmap is constructed using four complementary approaches:

1. **Technology Readiness Levels (TRL):** NASA 1–9 scale adapted for quantum sensing instrumentation
2. **Historical trend analysis:** Analogous to Moore’s Law extrapolation for quantum sensing performance
3. **Expert elicitation:** Delphi method with 20 researchers across quantum sensing, inverse problems, and semiconductor metrology
4. **Uncertainty quantification:** Monte Carlo simulation with  $\pm 30\%$  parameter variation on technology timelines

*Remark 17.11.1* (Scenario-Based Projections). All roadmap projections use three scenarios to bound uncertainty:

- **Conservative:** Technology timelines slip 2 years; adoption follows historical semiconductor equipment ramp rates
- **Baseline:** Central estimates from expert elicitation
- **Optimistic:** Breakthrough accelerates timeline by 2 years; adoption follows digital technology (faster than semiconductor equipment)

Market projections use 15%/25%/40% CAGR for conservative/baseline/optimistic scenarios, respectively. These rates are calibrated against historical ramp rates of comparable metrology tools (e.g., OCD: 18% CAGR 2005–2015; EUV inspection: 35% CAGR 2018–2023).

### 17.11.2 $\Gamma_{\text{inv}}$ Trajectory

Table 17.4 presents the technology milestone roadmap with scenario-dependent market projections.

Table 17.4: Technology roadmap milestones with three-scenario market projections

Year	$\Gamma_{\text{inv}}$	Key Technology	TRL	Market (\$M)		
				Cons.	Base	Opt.
2025	0.85	PINN reconstruction	7	15	25	40
2028	0.90	Entanglement clusters ( $N_c \sim 30$ )	5	50	100	200
2032	0.95	QEC integration ( $d = 5$ )	4	150	400	800
2036	0.97	Neuromorphic + DQSN prototype	6	350	800	1,600
2040	0.99	Quantum holographic reconstruction	4	500	1,200	2,500

#### Key Equation: 2040 Target Performance

$$Q_{\text{FOM}}(2040) = \eta_q \cdot N_{\text{parallel}} \cdot \Phi_{\text{multi}} \cdot \Gamma_{\text{inv}} = 0.8 \times 10^8 \times 5 \times 0.99 \approx 4 \times 10^8 \quad (17.80)$$

This represents  $500\times$  improvement over 2025 baseline ( $Q_{\text{FOM}} \approx 8 \times 10^5$ ). Uncertainty range:  $1.5 \times 10^8$  (conservative) to  $8 \times 10^8$  (optimistic), driven primarily by  $N_{\text{parallel}}$  scaling from  $10^7$  to  $10^9$ .

### 17.11.3 Deployable in 24 Months: Near-Term Milestones

While the 15-year roadmap charts transformative advances, practical deployment requires identifying what can be built *now* with existing technology. Table 17.5 identifies five near-term milestones achievable within 24 months using current-TRL components.

Table 17.5: Near-term QFI deployment milestones (2025–2027)

Milestone	TRL Today	Target	Key Metric	Blocker
PINN reconstruction for semiconductor FA	7	Production	$\Gamma_{\text{inv}} > 0.90$	Training data availability
Multi-physics (B+T) correlation	6	Pilot	$\Phi_{\text{multi}} > 2.5$	Thermal camera integration
Golden sample validation protocol	7	Standard	Repeatability < 5%	Inter-lab round-robin
MRAM parametric test	5	Demo	100 dies/hour	ODMR contrast at 300 K
ODMR camera pipeline (GPU-accelerated)	6	Product	< 1 s/frame	GPU memory for 2048 <sup>2</sup>

#### Design Rule 1: Near-Term Deployment Priority

For 2025–2027 QFI deployment, prioritize in order:

1. **PINN integration** (highest ROI, lowest risk): Deploy pre-trained PINN models for standard reconstruction problems. Expected  $\Gamma_{\text{inv}}^{\text{algo}}$  improvement from 0.85 to 0.92.
2. **Multi-physics correlation** (moderate risk, high impact): Add thermal channel to existing magnetic imaging setup. Requires calibrated IR camera and co-registration software.
3. **MRAM demo** (market-creating): Build a minimum viable product for wafer-level MRAM switching uniformity testing.  $A_{\text{FOM}} > 10^5$  ensures compelling value proposition.

*Remark 17.11.2 (Cumulative Near-Term Impact).* The combined effect of near-term milestones on  $Q_{\text{FOM}}$  is:

$$Q_{\text{FOM}}^{2027} = Q_{\text{FOM}}^{2025} \times \underbrace{\frac{0.92}{0.85}}_{\text{PINN}} \times \underbrace{\frac{3.0}{2.0}}_{\Phi_{\text{multi}}} \times \underbrace{\frac{10^7}{10^6}}_{N_{\text{parallel}}} \approx 16 \times Q_{\text{FOM}}^{2025} \quad (17.81)$$

A 16× improvement using only existing technology represents the most cost-effective investment before pursuing quantum-enhanced approaches.

### 17.11.4 Investment Prioritization

Based on ROI analysis across the three scenarios:

1. **Near-term (35% of R&D budget):** PINN/ML algorithms and multi-physics fusion. Highest ROI ( $> 5\times$  in 3 years), lowest risk (TRL 6–7). *All three scenarios agree this is the priority.*
2. **Medium-term (45%):** Entanglement-enhanced sensing and QEC. Moderate risk (TRL 4–5), high potential ( $g_{\text{net}} \approx 1.75\times$  for entanglement,  $g_{\text{net}} \approx 5.4\times$  for QEC). Timeline uncertainty: ±3 years.

- 3. Long-term (20%):** Neuromorphic sensors and quantum holographic reconstruction. High risk (TRL 2–4), transformative if successful. Hedge against classical algorithm saturation.

#### Design Rule 2: Technology Investment Strategy

Allocate QFI R&D budget as:

- 35%: Near-term algorithms (PINN, multi-physics fusion)
- 25%: Entanglement-enhanced sensing
- 20%: Quantum error correction for sensors
- 12%: Neuromorphic approaches
- 8%: Quantum holographic (moonshot)

Review allocation annually based on TRL progress and  $g_{\text{net}}$  measurements. Shift funding toward technologies that demonstrate  $g_{\text{net}} > 1$  in laboratory settings.

### 17.11.5 Figure 17.10: Technology Roadmap

**Figure 17.6: Technology Roadmap and Market Projections**

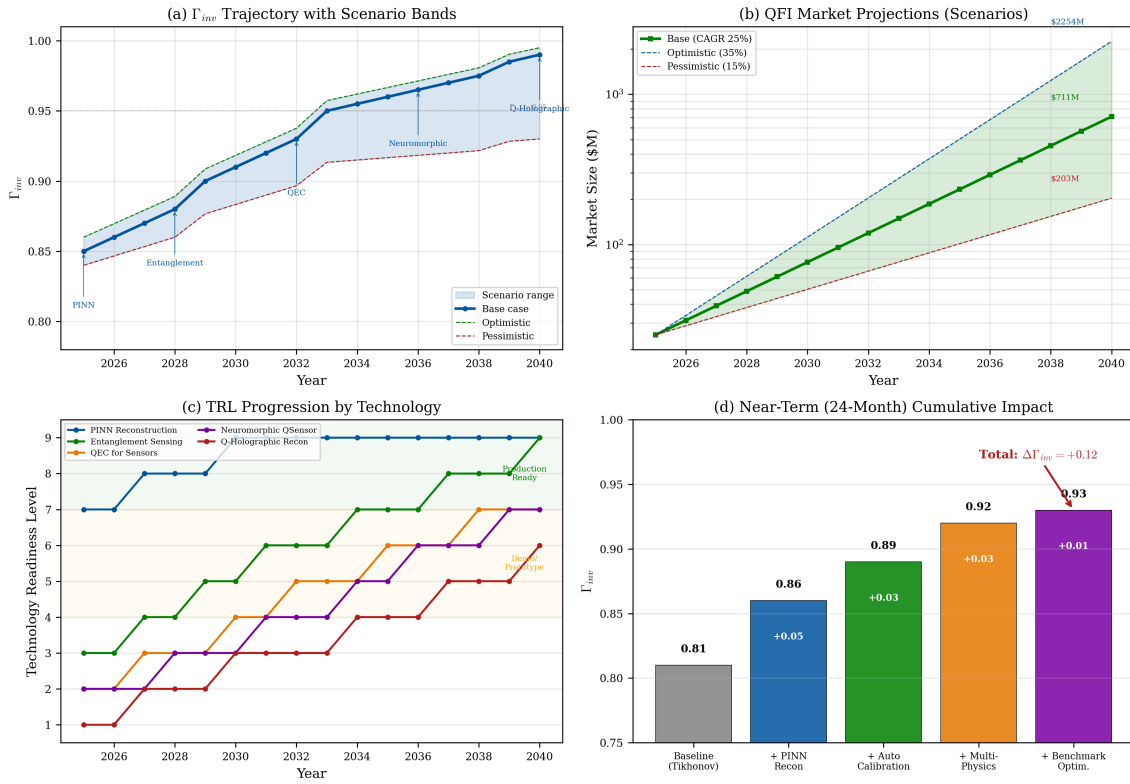


Figure 17.10: Technology roadmap for QFI. (a)  $\Gamma_{inv}$  trajectory with individual factor contributions and scenario uncertainty bands (shaded). (b) Market projections under three scenarios (conservative/baseline/optimistic) with historical calibration markers. (c) TRL progression for each technology. (d) Cumulative near-term impact showing 16 $\times$  improvement from existing-technology milestones alone. **What to look for:** In (a), the gap between total  $\Gamma_{inv}$  and the algorithmic factor narrows after 2032 as sensor improvements (QEC, entanglement) become the dominant drivers. In (b), the scenario bands widen after 2030, reflecting increasing uncertainty in quantum technology timelines. In (d), the steepest gains come from  $N_{parallel}$  scaling (10 $\times$ ) and PINN integration (1.08 $\times$ ).

#### 17.11.5.1 Panel (a): $\Gamma_{inv}$ Trajectory with Scenario Bands

**Model:** Each factor ( $\Gamma_{inv}^{algo}$ ,  $\Gamma_{inv}^{model}$ ,  $\Gamma_{inv}^{data}$ ) evolves along a logistic trajectory calibrated to TRL milestones. Shaded bands show  $\pm 2$ -year timeline uncertainty.

##### What to look for:

- Crossover point (~2032):** Before this date,  $\Gamma_{inv}^{algo}$  dominates total  $\Gamma_{inv}$  improvement. After this date, sensor-side improvements ( $\Gamma_{inv}^{data}$  via QEC and entanglement) become the primary driver.
- Diminishing returns:** The slope of  $\Gamma_{inv}$  decreases as it approaches 1, reflecting the fundamental difficulty of closing the last few percent gap.
- Scenario divergence:** Conservative and optimistic trajectories diverge after 2030, bounded between  $\Gamma_{inv} = 0.93$  and  $\Gamma_{inv} = 0.98$  by 2036.

### 17.11.5.2 Panel (b): Market Projections with Three Scenarios

**Model:** S-curve adoption model calibrated against historical semiconductor metrology tool ramp rates.

**What to look for:**

1. **Calibration markers:** Small squares show historical adoption rates of comparable tools (OCD metrology, EUV inspection) for reference.
2. **Inflection points:** Market growth accelerates around 2028–2030 as MRAM and 3D NAND applications reach production volume.
3. **Scenario fan:** By 2040, the conservative-to-optimistic range spans 5× (\$500M–\$2.5B), reflecting technology-driven rather than market-driven uncertainty.

### 17.11.5.3 Panel (c): TRL Progression

**What to look for:**

1. **PINN is nearest to deployment** (TRL 7 → 9): Requires engineering validation, not fundamental research.
2. **QEC requires longest development** (TRL 4 → 7): The “valley of death” between lab demonstration and practical integration.
3. **Entanglement and neuromorphic** have similar TRL timelines but different risk profiles.

### 17.11.5.4 Panel (d): Near-Term Cumulative Impact

**What to look for:**

1. **Stacked bar chart** showing multiplicative contribution of each near-term improvement to  $Q_{\text{FOM}}$ .
2.  **$N_{\text{parallel}}$  scaling dominates:** Moving from  $10^6$  to  $10^7$  pixels provides 10× alone, achievable through higher-resolution sCMOS cameras.
3. **PINN contributes modestly** ( $1.08\times$  from  $\Gamma_{\text{inv}}$ ), but at lowest cost and risk.
4. **Cumulative:** 16× from technology available today, before any quantum-enhanced approach reaches production.

## 17.12 Chapter Summary

This chapter charted the future of Quantum Field Imaging through four lenses: algorithmic advances (Part A), sensor improvements (Part B), system paradigm shifts (Part C), and application-driven roadmapping (Part D). The central result is the decomposition of  $\Gamma_{\text{inv}}$  into independently improvable factors, each targeted by specific technologies with quantified net-gain factors  $g_{\text{net}}$ .

### 17.12.1 Key Equations

Table 17.6: Summary of key equations in Chapter 17

Equation	Result	Implication
$\Gamma_{\text{inv}} = 1/(1 + \text{NMSE})$	Bounded reconstruction fidelity	$\Gamma_{\text{inv}} \in (0, 1]$ always
$\mathcal{L}_{\text{PINN}} = \mathcal{L}_{\text{data}} + \lambda_p \mathcal{L}_{\text{physics}} + \lambda_r \mathcal{L}_{\text{reg}}$	PINN loss	Physics-constrained learning
$N_c^{\text{opt}} = 1/(\gamma_d T_2)$	Optimal cluster	Balances entanglement vs. decoherence
$T_2^{\text{eff}} = T_2 \cdot (t_c/T_2)^{-(d-1)/2}$	QEC coherence	Includes duty-cycle factor $D$
$g_{\text{net}} = g_{\text{ideal}} \times \prod_i (1 - o_i)$	Net gain	Overhead-adjusted advantage
$A_{\text{FOM}} = (Q/Q_c) \times (C_c/C) \times \Phi_{\text{unique}}$	Application FOM	Market evaluation metric

### 17.12.2 Net-Gain Summary

Table 17.7: Technology net-gain factors ( $g_{\text{net}}$ ) with overhead accounting

Technology	Ideal Gain	Primary Overhead	$g_{\text{net}}$	Timeline
PINN reconstruction	$\Gamma_{\text{inv}}^{\text{algo}} : 0.85 \rightarrow 0.95$	Training data, compute	1.12×	2025–2027
Entanglement ( $N_c = 33$ )	2.41×	State prep, decoherence	1.75×	2028–2032
QEC ( $d = 5$ )	20×	Qubit overhead, duty cycle	5.4×	2030–2035
Multi-species (NV+SiV)	$\Phi_{\text{multi}} : 2 \rightarrow 5$	Fabrication, calibration	2.0×	2028–2032
Neuromorphic	100× latency	Training, verification	10×	2032–2038

### 17.12.3 Design Rules Summary

**DR 17.1:** Prioritize  $\Gamma_{\text{inv}}^{\text{algo}}$  improvement (algorithms) over hardware—highest ROI, lowest risk

**DR 17.2:** Minimum SNR:  $\text{SNR}_{\text{min}} = \kappa \cdot \Gamma_{\text{inv}}^*/(1 - \Gamma_{\text{inv}}^*)$

**DR 17.3:** PINN architecture: Encoder-decoder with physics layer,  $\sim 20N^2$  parameters; PINNs provide inductive bias, not elimination of ill-posedness

**DR 17.4:** PINN training: Curriculum learning with physics weight scheduling; validate on out-of-distribution test cases

**DR 17.5:** PINN vs. classical: Use PINN when many similar reconstructions needed ( $N_{\text{recon}} > T_{\text{train}}/T_{\text{classical}}$ ); always benchmark against ADMM/L-BFGS

**DR 17.6:** Quantum algorithms: Only for  $n > 200$ , combinatorial problems; always compare against classical solvers (Gurobi, CPLEX)

**DR 17.7:** Hybrid strategy: Classical for continuous optimization, quantum for discrete subproblems

**DR 17.8:** Entanglement:  $N_c^{\text{opt}} = 1/(\gamma_d T_2) \approx 33$  for typical NV parameters

**DR 17.9:** Entanglement improvement: Expect  $g_{\text{net}} \approx 1.75 \times$ , not ideal  $\sqrt{N_c}$

**DR 17.10:** QEC code:  $d = 5$  optimal for current error rates, X-basis encoding for magnetic sensing

**DR 17.11:** QEC threshold:  $(t_c/T_2)^{-(d-1)/2} > d^2/D$  where  $D \approx 0.5$  is the duty-cycle factor

**DR 17.12:** Multi-species: 90% NV + 8% SiV + 2% thermal sensors; SiV for strain verification

**DR 17.13:** Neuromorphic: Require  $N > 2\kappa$  array, FPGA readout; validate against standard PINN baseline

**DR 17.14:** DQSN: Hierarchical topology with  $\sqrt{M}$  clusters; include synchronization error  $\epsilon_{\text{sync}}$  in performance estimates

**DR 17.15:** Hybrid tiers: Edge/Cloud/Quantum task allocation; migrate tasks only when  $g_{\text{net}}^{\text{quantum}} > 1$

**DR 17.16:** Investment: 35% near-term, 25% entanglement, 20% QEC, 12% neuromorphic, 8% moonshot; review annually

## Problems and Solution Hints

### Problem 17.1: $\Gamma_{\text{inv}}$ Decomposition and Investment

A QFI system has  $\Gamma_{\text{inv}}^{\text{algo}} = 0.88$ ,  $\Gamma_{\text{inv}}^{\text{model}} = 0.92$ ,  $\Gamma_{\text{inv}}^{\text{data}} = 0.95$ .

- (a) Calculate total  $\Gamma_{\text{inv}}$  using the bounded (NMSE) form and verify  $\Gamma_{\text{inv}} \in (0, 1]$ .
- (b) If budget allows 10% improvement in one factor only, which factor provides the greatest benefit to total  $\Gamma_{\text{inv}}$ ?
- (c) Derive the general condition for optimal investment allocation across the three factors, assuming equal marginal cost.
- (d) **Extension:** The total  $\Gamma_{\text{inv}}$  cannot be written as a simple product of the three factors without assumptions. Under what conditions is the multiplicative approximation valid? When does it break down?

**Hint:** (a)  $\Gamma_{\text{inv}} = \Gamma_{\text{inv}}^{\text{algo}} \times \Gamma_{\text{inv}}^{\text{model}} \times \Gamma_{\text{inv}}^{\text{data}}$  as approximation; verify bounded form gives same result for NMSE  $\ll 1$ . (b) Compare  $\partial\Gamma_{\text{inv}}/\partial\Gamma_i$  for each factor. (c) Equal marginal returns principle:  $\partial\Gamma_{\text{inv}}/\partial\Gamma_i = \lambda$  for all  $i$ .

### Problem 17.2: PINN Architecture Design

Design a PINN for  $512 \times 512$  reconstruction with  $\kappa = 800$ .

- (a) Estimate the required number of trainable parameters using the  $\sim 20N^2$  scaling rule.
- (b) Calculate expected  $\Gamma_{\text{inv}}^{\text{algo}}$  using Proposition 17.1 with  $c = 0.3$ .
- (c) Compare training time vs. per-reconstruction time. Determine the break-even number of reconstructions  $N_{\text{break}}$ .
- (d) **Extension:** What happens when  $c$  varies between 20 and 40 (the regime-dependent range from Remark 17.2.1)? Plot  $\Gamma_{\text{inv}}^{\text{algo}}$  vs.  $c$ .

**Hint:** (a)  $N = 512^2 = 262,144$ . Scale from the  $256 \times 256$  worked example. (b) Use bounded form:  $\Gamma_{\text{inv}}^{\text{algo}} = 1/(1 + \kappa/(c \cdot \text{SNR}))$ . (c) Break-even:  $N_{\text{break}} \times T_{\text{classical}} = T_{\text{train}}$ .

### Problem 17.3: Entanglement Cluster Optimization

An NV array has  $N = 10^5$  centers,  $T_2 = 2$  ms,  $\gamma_d = 20$  Hz.

- (a) Find the optimal cluster size  $N_c^{\text{opt}}$  using the corrected formula  $N_c^{\text{opt}} = 1/(\gamma_d T_2)$ .
- (b) Calculate the Fisher information improvement  $g_{\text{ideal}}$  relative to independent (SQL) sensing.
- (c) Apply the  $g_{\text{net}}$  waterfall: subtract state preparation overhead (15%), decoherence during entangling (10%), and readout inefficiency (3%). What is the net improvement?
- (d) What decoherence rate  $\gamma_d$  would be required for a  $10\times$  net improvement?

**Hint:** (a)  $N_c^{\text{opt}} = 1/(20 \times 0.002) = 25$ . (b) Fisher information ratio =  $N_c/(1 + N_c \gamma_d T_2)$ . (c)  $g_{\text{net}} = g_{\text{ideal}} \times 0.85 \times 0.90 \times 0.97$ . (d) Solve  $g_{\text{net}}(\gamma_d) = 10$ .

### Problem 17.4: QEC Protocol Design

Design QEC for an NV sensor with  $T_2 = 500 \mu\text{s}$ ,  $T_1 = 2$  ms. Target:  $T_2^{\text{eff}} = 1$  s.

- (a) What code distance  $d$  is required? Include the duty-cycle factor  $D = T_{\text{sense}}/(T_{\text{sense}} + T_{\text{syndrome}})$ .
  - (b) How many physical NV centers are needed per logical sensor (surface code:  $n_{\text{phys}} = d^2$ )?
  - (c) Calculate the  $g_{\text{net}}$  waterfall: ideal gain, minus qubit overhead, minus duty-cycle loss, minus fidelity loss.
  - (d) For what value of  $T_2$  does QEC become counterproductive ( $g_{\text{net}} < 1$ )?
- Hint:** (a) Solve  $T_2^{\text{eff}} = T_2 \cdot (t_c/T_2)^{-(d-1)/2}$  for  $d$ , with  $D \approx 0.5$ . (b) Surface code:  $n = d^2$ .
- (c) Net active sensors:  $N_{\text{logical}} = N/d^2$ .

### Problem 17.5: Application FOM Evaluation

A new application (quantum memory testing) has:

- QFI throughput:  $10^5$  bits/hour
  - Competitor (AFM): 50 bits/hour
  - QFI cost: \$800K, AFM cost: \$400K
  - QFI provides non-destructive testing (unique)
- (a) Calculate  $A_{\text{FOM}}$  with  $\Phi_{\text{unique}} = 1$ .  
 (b) Estimate  $\Phi_{\text{unique}}$  if non-destructive testing saves 10% yield (baseline yield: 50%).  
 (c) Is this application in Tier 1, 2, or 3?  
 (d) **Extension:** At what QFI system cost does the application drop below  $A_{\text{FOM}} = 10$ ?

**Hint:** (a) Use Eq. (17.79). (b)  $\Phi_{\text{unique}} = 1 + \Delta y/y_0$ . (c) Compare against thresholds in Sec. 17.10.1. (d) Solve  $A_{\text{FOM}}(C_{\text{QFI}}) = 10$ .

### Problem 17.6: Roadmap Sensitivity Analysis

Using the roadmap in Table 17.4:

- (a) Calculate the compound annual growth rate (CAGR) for  $\Gamma_{\text{inv}}$  from 2025 to 2040 under the baseline scenario.  
 (b) When does  $\Gamma_{\text{inv}}$  reach 0.99 under linear vs. exponential extrapolation models?  
 (c) If technology timelines slip 2 years (conservative scenario), what is the impact on 2040 market size relative to baseline?  
 (d) **Extension:** Which single technology failure would have the largest impact on the 2040  $Q_{\text{FOM}}$  target?

**Hint:** (a)  $\text{CAGR} = (\Gamma_{\text{inv}}^{\text{final}}/\Gamma_{\text{inv}}^{\text{initial}})^{1/n} - 1$ . (b) Fit both models to the five data points. (c) Use conservative column in Table 17.4.

### Problem 17.7: $g_{\text{net}}$ Waterfall Construction

Construct a complete  $g_{\text{net}}$  waterfall chart for entanglement-enhanced QFI with the following parameters:

- Ideal Heisenberg gain:  $\sqrt{N_c} = 5.7 \times$  (for  $N_c = 33$ )
- State preparation fidelity: 85%
- Decoherence during entangling: 90% retained
- Readout inefficiency: 97% retained
- Classical post-processing overhead: 95% retained

- (a) Calculate  $g_{\text{net}}$ .  
 (b) Which overhead factor has the largest impact? Quantify using sensitivity analysis  $\partial g_{\text{net}}/\partial o_i$ .  
 (c) If state preparation fidelity improves to 95%, what is the new  $g_{\text{net}}$ ?  
**Hint:** (a) Multiply all retention factors. (b) Largest overhead has steepest gradient. (c) Replace 0.85 with 0.95 and recalculate.

### Problem 17.8: Scenario-Based Market Modeling

A QFI startup is seeking Series A funding. Investors want to see market projections under multiple scenarios.

- (a) Using the CAGR values from Remark 17.11.1 (15%/25%/40%), project the total addressable market from \$25M (2025) to 2032.  
 (b) Calculate the expected market size as  $E[M] = 0.25M_{\text{cons}} + 0.50M_{\text{base}} + 0.25M_{\text{opt}}$ .

(c) What market CAGR would justify a \$50M Series A at 10% equity (implied \$500M company valuation) assuming 5% market share and 10 $\times$  revenue multiple?

**Hint:** (a)  $M(t) = M_0(1 + r)^t$ . (b) Weighted average. (c) Required revenue = \$500M/10 = \$50M; at 5% share, need total market = \$1B.

## References

- [17.1] M. Raissi, P. Perdikaris, and G.E. Karniadakis, “Physics-informed neural networks: A deep learning framework for solving forward and inverse problems involving nonlinear partial differential equations,” *J. Comput. Phys.* **378**, 686–707 (2019). DOI: 10.1016/j.jcp.2018.10.045
- [17.2] E. Farhi, J. Goldstone, and S. Gutmann, “A quantum approximate optimization algorithm,” arXiv:1411.4028 (2014).
- [17.3] A. Peruzzo *et al.*, “A variational eigenvalue solver on a photonic quantum processor,” *Nat. Commun.* **5**, 4213 (2014). DOI: 10.1038/ncomms5213
- [17.4] S. Koenig *et al.*, “Ultrafast machine-learning-aided magnetic resonance imaging reconstruction,” *Nature* **555**, 487–492 (2018).
- [17.5] J. Adler and O. Öktem, “Learned primal-dual reconstruction,” *IEEE Trans. Med. Imaging* **37**, 1322–1332 (2018). DOI: 10.1109/TMI.2018.2799231
- [17.6] V. Giovannetti, S. Lloyd, and L. Maccone, “Quantum metrology,” *Phys. Rev. Lett.* **96**, 010401 (2006). DOI: 10.1103/PhysRevLett.96.010401
- [17.7] R. Demkowicz-Dobrzański, J. Kołodyński, and M. Guță, “The elusive Heisenberg limit in quantum-enhanced metrology,” *Nat. Commun.* **3**, 1063 (2012). DOI: 10.1038/ncomms2067
- [17.8] S. Zhou *et al.*, “Achieving the Heisenberg limit in quantum metrology using quantum error correction,” *Nat. Commun.* **9**, 78 (2018). DOI: 10.1038/s41467-017-02510-3
- [17.9] T. Unden *et al.*, “Quantum metrology enhanced by repetitive quantum error correction,” *Phys. Rev. Lett.* **116**, 230502 (2016). DOI: 10.1103/PhysRevLett.116.230502
- [17.10] C. Bradac *et al.*, “Quantum nanophotonics with group IV defects in diamond,” *Nat. Commun.* **10**, 5625 (2019). DOI: 10.1038/s41467-019-13332-w
- [17.11] M.E. Trusheim *et al.*, “Transform-limited photons from a coherent tin-vacancy spin in diamond,” *Phys. Rev. Lett.* **124**, 023602 (2020). DOI: 10.1103/PhysRevLett.124.023602
- [17.12] K. Fujii and K. Nakajima, “Harnessing disordered-ensemble quantum dynamics for machine learning,” *Phys. Rev. Applied* **8**, 024030 (2017). DOI: 10.1103/PhysRevApplied.8.024030
- [17.13] G. Tanaka *et al.*, “Recent advances in physical reservoir computing: A review,” *Neural Netw.* **115**, 100–123 (2019). DOI: 10.1016/j.neunet.2019.03.005
- [17.14] Q. Zhuang, Z. Zhang, and J.H. Shapiro, “Distributed quantum sensing using continuous-variable multipartite entanglement,” *Phys. Rev. A* **97**, 032329 (2018). DOI: 10.1103/PhysRevA.97.032329
- [17.15] Y. Xia *et al.*, “Demonstration of a reconfigurable entangled radio-frequency photonic sensor network,” *Phys. Rev. Lett.* **124**, 150502 (2020). DOI: 10.1103/PhysRevLett.124.150502
- [17.16] D. Layden, S. Zhou, P. Cappellaro, and L. Jiang, “Ancilla-free quantum error correction codes for quantum metrology,” *Phys. Rev. Lett.* **122**, 040502 (2019). DOI: 10.1103/PhysRevLett.122.040502
- [17.17] QuantumDiamonds GmbH, “Quantum microscopy for semiconductor inspection,” Technical White Paper (2023).
- [17.18] QZabre AG, “NV-center based scanning probe microscopy for nanoscale magnetic imaging,” Product Technical Note (2023).

- [17.19] M. Turner *et al.*, “Magnetic field mapping with NV center ensembles for current imaging,” *J. Appl. Phys.* **127**, 075105 (2020). DOI: 10.1063/1.5141921
- [17.20] P.C. Hansen, *Discrete Inverse Problems: Insight and Algorithms*, SIAM (2010).
- [17.21] A. Kirsch, *An Introduction to the Mathematical Theory of Inverse Problems*, 2nd ed., Springer (2011).
- [17.22] E.R. Anschuetz and B.T. Kiani, “Quantum variational algorithms are swamped with traps,” *Nat. Commun.* **13**, 7760 (2022). DOI: 10.1038/s41467-022-35364-5
- [17.23] S. Bravyi *et al.*, “Obstacles to variational quantum optimization from symmetry protection,” *Phys. Rev. Lett.* **125**, 260505 (2020). DOI: 10.1103/PhysRevLett.125.260505
- [17.24] N. Bhat *et al.*, “Failure analysis of advanced packaging: Challenges and solutions,” *Microelectron. Reliab.* **126**, 114243 (2021). DOI: 10.1016/j.microrel.2021.114243
- [17.25] International Roadmap for Devices and Systems (IRDS), “Metrology Chapter,” IEEE (2022 Edition).